Target Detection through Quantum Illumination

by

Sara L. Mouradian

S.B. EECS, M.I.T., 2010

Submitted to the Department of Electrical Engineering and Computer Science
in partial fulfillment of the requirements for the degree of

Master of Engineering in Electrical Engineering and Computer Science

at the

MASSACHUSETTS INSTITUTE OF TECHNOLOGY

February 2012

Author .....
Department of Electrical Engineering and Computer Science
February 1 2012

Certified by .....
Dr. Franco N.C. Wong, Senior Research Scientist
Thesis Supervisor

Accepted by .....
Prof. Dennis M. Freeman
Chairman, Master of Engineering Thesis Committee

Target Detection through Quantum Illumination

by

Sara L. Mouradian

Submitted to the Department of Electrical Engineering and Computer Science
on February 1 2012, in partial fulfillment of the
requirements for the degree of
Master of Engineering in Electrical Engineering and Computer Science

Abstract

Classical target detection can suffer large error probabilities in noisy and lossy environments when noise photons are mistaken for signal photons reflected from an object. It has been shown theoretically that the correlation between entangled photons can be used to better discriminate between the signal photons reflected by an object and noise photons, thus reducing the probability of error [13, 15, 17, 7, 6].

This thesis presents the first experimental implementation of target detection enhanced by quantum illumination (QI). Nondegenerate, time entangled signal and idler beams are created through Type-0 spontaneous parametric downconversion (SPDC). The signal is attenuated and combined with large levels of noise. The signal is phase modulated to improve the observation by shifting it from DC to 16 kHz. The return signal and idler are recombined in an optical parametric amplifier (OPA) which captures the phase correlation between the two beams.

It is found that only 10% of the total signal and idler photons interact at the OPA due to the multi-mode nature of the SPDC emission which does not match the pump spatial mode and thus experience lower gains at the OPA. Considering only the power interacting at the OPA, the signal-to-noise ratio (SNR) of QI agrees with the theoretical model.

Thesis Supervisor: Dr. Franco N.C. Wong,
Title: Senior Research Scientist

Acknowledgments

I would like to first thank Dr. Franco Wong for all his mentorship, advice, and patience. Under his guidance I have moved beyond a student, and now can call myself a researcher. I would also like to thank Maria Tengner for providing endless hands-on advice in the lab. Most importantly, I would like to thank her for remaining calm and collected at all times, helping me retain perspective and objectivity through all road blocks. I'd like to thank my parents for making this opportunity possible and supporting me through everything. Finally, I'd like to thank my friends for their boundless emotional support.

Contents

List of Figures

Chapter 1

Introduction

Optical entanglement, a greater-than-classical correlation between a pair of photons, is a standard resource in quantum optics. Spontaneous parametric downcoversion (SPDC) is widely used to create spectrally bright sources of entangled photons in the laboratory. This entangled light has fueled advances in quantum computing [16], cryptography [8], and metrology [5]. Unfortunately, the quantum levels of entanglement are easily degraded by noise and loss. Outside of a controlled laboratory setting optical signals ubiquitously suffer absorption loss, atmospheric turbulence, and the addition of noise—all of which degrade the correlation between entangled photons. Thus, applications of entanglement outside of a controlled environment have, until now, been limited.

Surprisingly, recent theoretical work has suggested that entanglement can provide advantages over classical light in environments with high levels of loss and noise. One application is low power target detection in noisy and lossy environments.

In optical target detection, light is transmitted to the region of interest. If an object is present in this region, the light is reflected and this return light will be detected at the receiver. Thus, if light is incident on the receiver, it is hypothesized that a target is present. If no light is detected, it is hypothesized that there is no target present. With large transmitted power and an environment with low loss and noise, the probability of these hypotheses being false is low. However, if noise photons overwhelm the original signal photons at the receiver due to low initial power, high

loss, and high noise, the probability of error increases as noise photons are detected at the receiver, implying that an object is present even if it is not.

Entanglement can be used to better distinguish between noise photons and signal photons, decreasing the probability of error. This is quantum illumination as applied to target detection. Half of an entangled beam (the signal) is sent to interrogate the target region while the other half (the idler) is retained for use in a phase sensitive joint measurement on the return signal as seen in Fig. 1-1. Because the signal and idler are entangled, the noise photons are less likely to masquerade as signal photons as they can in simple target detection.

This thesis presents experimental results in support of the theoretical increase in the signal-to-noise ratio when using quantum illumination over classical target detection. In the setup, SPDC is used to create pairs of nondegenerate time-entangled photons. The signal and idler beams are separated and the signal path is subjected to noise and loss. The beams are recombined in an optical parametric amplifier as the quantum receiver and the output is detected with an avalanche photodiode with a low noise, high gain transimpedance amplifier.

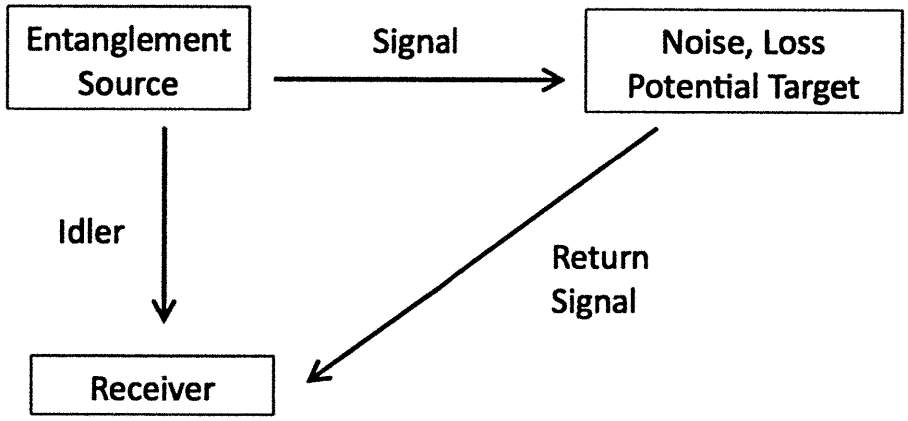

Figure 1-1: A basic schematic of the experiment presented in this thesis.

Chapter 2

Theory

The theory behind quantum illumination as applied to target detection has been developed through a series of papers—[13, 15, 17, 7, 6]. Here, the basic calculations and conclusions of these papers are presented. The conclusions are then extended to take into account experimental parameters.

2.1 Theoretical Background

Quantum illumination (QI) was first introduced by Seth Lloyd in 2008 [13]. In this initial paper, Lloyd studies the simplest theoretical setup. In both the classical and quantum cases the transmitted signal consists of a series of discrete one-photon packets. Only one photon arrives at the detector at each time bin—either a noise photon or a signal photon. Multiple trials are performed until the distributions present at the detector with and without a target present can be separated. With QI, each incoming photon is measured with the retained idler photon to determine if the two photons are entangled. The returning signal photon will always match the phase-conjugate idler photon as they are entangled. On the other hand, a noise photon is d times less likely to be found in the state of the ancilla, where d is the number of modes captured per detection event. Thus, Lloyd finds that entanglement reduces the effective noise, and hence increases the signal to noise ratio, by a factor of d in a noisy environment [13]. This is especially interesting because the large amount of noise and loss in the

transmission means that the signal and idler are no longer entangled at the receiver in the quantum sense—however, they are still correlated and thus it is difficult for a noise photon to masquerade as a signal photon.

While Lloyd's analysis does show that entanglement provides a clear enhancement in that particular scenario, it does not represent a realistic or implementable situation. In fact, in a paper published in 2009, Shapiro and Lloyd show that the single-photon QI scheme put forth in [13] cannot compete against a coherent-state classical source of the same average photon number [15]. Nevertheless, they point to a paper published by Tan *et al.* soon after the original Lloyd paper that provides a full Gaussian-state treatment of quantum illumination [17].

Instead of working in the theoretical realm of single photon and vacuum state statistics, Tan *et al.* consider the full quantum statistics for entangled signal and idler beams created by spontaneous parametric downconversion (SPDC) through continuous wave pumping of a nonlinear crystal—a situation readily realizable in a quantum optics laboratory. Each signal and idler mode created by SPDC has a mean photon-pair number $N_s \ll 1$ and is in a maximally entangled zero-mean Gaussian state. The full quantum description of a bright thermal noise bath with a mean photon number of $N_b \gg 1$ in each mode is considered. The theory in [17] underpins the experiment presented in this thesis.

To understand the effect of entanglement on the target detection system, the Wigner-distribution covariance matrix between the return signal and the retained idler is computed at the receiver for the classical and quantum cases. The Wigner-distribution covariance matrix is a measure of the correlation between the quadratures of two signals $\hat{a}_a = \hat{a}_{a_1} + i\hat{a}_{a_2}$ and $\hat{a}_b = \hat{a}_{b_1} + i\hat{a}_{b_2}$ and is given by $\Lambda_{ab} = \langle [\hat{a}_{a_1}\hat{a}_{a_2}\hat{a}_{b_1}\hat{a}_{b_2}]^T [\hat{a}_{a_1}\hat{a}_{a_2}\hat{a}_{b_1}\hat{a}_{b_2}] \rangle$.

As expected, the Wigner distribution covariance matrix of the initial signal and

idler beams shows maximal entanglement in the off-diagonal elements

$$\Lambda_{si} = \frac{1}{4}\begin{bmatrix} 2N_s+1 & 0 & 2\sqrt{N_s(N_s+1)} & 0 \\ 0 & 2N_s+1 & 0 & -2\sqrt{N_s(N_s+1)} \\ 2\sqrt{N_s(N_s+1)} & 0 & 2N_s+1 & 0 \\ 0 & -2\sqrt{N_s(N_s+1)} & 0 & 2N_s+1 \end{bmatrix} \tag{2.1}$$

The idler is retained for the joint measurement at the detector. In this initial theoretical treatment of the situation, it is assumed that the idler experiences no loss. The signal is sent to interrogate the target region. The path is lossy and bathed in bright thermal noise. If the target is not present (hypothesis 0), the return signal is comprised entirely of noise photons and the Wigner distribution covariance matrix between the return signal and the idler beams shows no correlation.

$$\Lambda_{r_0 i} = \frac{1}{4}\begin{bmatrix} 2N_s+1 & 0 & 0 & 0 \\ 0 & 2N_s+1 & 0 & 0 \\ 0 & 0 & 2N_b+1 & 0 \\ 0 & 0 & 0 & 2N_b+1 \end{bmatrix} \tag{2.2}$$

However, if the target is present (hypothesis 1), the noise is incorporated into the signal through a beamsplitter with a κ transmission giving a return signal of $\hat{a}_r = \sqrt{\kappa}\hat{a}_s + \sqrt{1-\kappa}\hat{a}_b$. In this case, the number of noise photons per mode is $\langle \hat{a}_b^\dagger \hat{a}_b \rangle = N_b/(1-\kappa)$ such that the total noise power at the detector is the same (N_b) regardless of the presence of a target. The Wigner distribution covariance matrix between the return signal and the idler beams is given by

$$\Lambda_{r_1 i} = \frac{1}{4}\begin{bmatrix} 2(\kappa N_s + N_b)+1 & 0 & 2\sqrt{\kappa N_s(N_s+1)} & 0 \\ 0 & 2(\kappa N_s + N_b)+1 & 0 & -2\sqrt{\kappa N_s(N_s+1)} \\ 2\sqrt{\kappa N_s(N_s+1)} & 0 & 2N_s+1 & 0 \\ 0 & -2\sqrt{\kappa N_s(N_s+1)} & 0 & 2N_s+1 \end{bmatrix} \tag{2.3}$$

The non-zero off-diagonal elements show that there is correlation between the

retained idler and the return signal when a target is present. In high noise and high loss situations ($N_b \geq \kappa$) the correlation does not exceed the classical upper bound on phase-sensitive cross correlations between each mode pair, $|\langle \hat{a}_{r_m} \hat{a}_{i_m} \rangle| \leq \sqrt{\langle \hat{a}^\dagger_{r_m} \hat{a}_{r_m} \rangle \langle \hat{a}^\dagger_{i_m} \hat{a}_{i_m} \rangle}$. Even so, there is no way to achieve this level of correlation at the receiver if starting with a classical state with the same amount of signal power. When using the classical state most analogous to the mode pairs created by SPDC, the off-diagonal Wigner-distribution covariance matrix elements are $|\langle \hat{a}_{r_m} \hat{a}_{i_m} \rangle| = \sqrt{\kappa N_s}/4$. In low-brightness operation ($N_s \ll 1$), this cross-correlation is less than that provided by quantum illumination $|\langle \hat{a}_{r_m} \hat{a}_{i_m} \rangle| = \pm 2\sqrt{\kappa N_s (N_s + 1)}$ as seen in the off-diagonal cross-correlation terms in Eq. 2.3. Thus, quantum illumination provides a phase-sensitive cross-correlation signature that is unattainable through classical means.

In [17], Tan *et al.* do not discuss receivers for capturing the phase sensitive cross-correlation between the return signal and idler. In two papers, Saikat Guha extends [17] with a full treatment of the statistics obtained from possible receivers [7, 6]. An optimal quantum receiver could detect the full cross correlation between the return signal and the retained idler. Unfortunately, an experimental implementation of this quantum receiver has not yet been developed. The best experimentally realizable receiver for detecting the phase sensitive cross correlation between the return signal and retained idler is the optical parametric amplifier (OPA) in conjunction with direct detection. The signal to noise ratio expected from this detection system is discussed in Section 2.2 and the implementation is discussed in Section 3.6. For classical target detection, balanced homodyne detection provides the optimal signal to noise ratio.

The theory presented in [6] explores the error probabilities—$P(0|1)$ and $P(1|0)$ for quantum illumination with an optimal quantum receiver, quantum illumination with an OPA receiver, and classical illumination using balanced homodyne detection.

It is found that the three scenarios differ in the exponent of the error probability,

$$\Pr(\text{error}) = \begin{cases} e^{(-M\kappa N_s/N_B)} & \text{QI \& an optimal quantum receiver} \\ e^{(-M\kappa N_s/2N_B)} & \text{QI \& OPA with direct detection} \\ e^{(-M\kappa N_s/4N_B)} & \text{Classical illumination \& homodyne detection[6]} \end{cases} \tag{2.4}$$

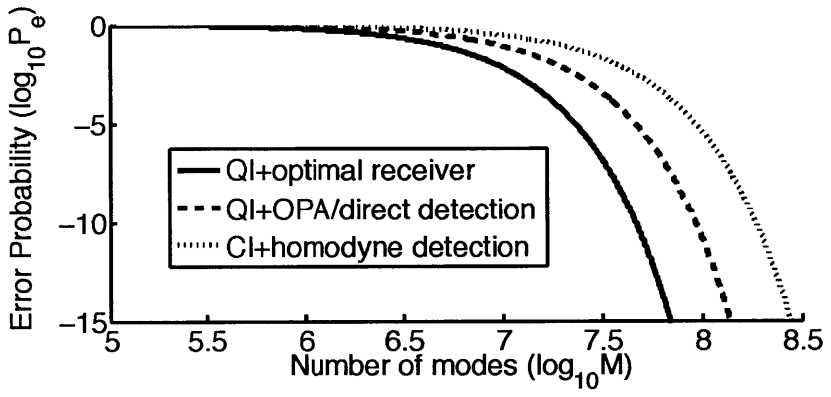

Figure 2-1: Error probabilities P_e for classical and quantum illumination with $N_s = 0.005$, $N_b = 100$, and $\kappa = 0.01$.

N_s, κ, and N_B are as described above, and M is the number of modes per detection period. Fig 2-1 shows these error exponents plotted against M at $N_s = 0.005$ photons/mode, $N_b = 100$ photons/mode, and $\kappa = 0.01$. It is clear that quantum illumination provides distinct advantages over classical illumination, especially when there are many modes in each detection period.

2.2 Optical Parametric Amplifier as Joint Receiver

As mentioned in Section 2.1, an optical parametric amplifier (OPA) is the optimal realizable receiver for capturing the phase sensitive cross-correlation between the retained idler and the return signal in quantum illumination. In the theoretical papers supporting this thesis discussed in Section 2.1, the error probability exponents are compared for the classical and quantum cases to reveal an advantaged gained through

using quantum illumination. In an experimental setup, it is more natural to compare the signal to noise ratios (SNRs) of classical and quantum illumination. In this section, the SNR of the output of the OPA is examined. All possibilities for loss are considered. $(1-\kappa)N_s$ signal photons per mode and $(1-\mu)N_s$ idler photons per mode are lost in transit. Furthermore, it is not assumed that the noise spectrum is constant over the bandwidth of interest. Instead, there are N_b/χ noise photons in χM modes, and zeros noise photons in the other $(1-\chi)M$ modes.

2.2.1 OPA Output

An optical parametric amplifier is created by focusing the pump (p) beam, idler (i), and return signal (s) into a nonlinear crystal. Due to nonlinear interactions, energy from the pump beam is transferred to or from the signal and idler wavelengths depending on the relative phase $\phi_p - \phi_s - \phi_i$. In the following we assume the phases are set so that the OPA operates as an amplifier. For each mode k of the return signal and the idler sent into the crystal, a pair of modes is created by the OPA—one at the idler wavelength, and one at the signal wavelength with mode creation operators $\hat{c}_k$ and $\hat{d}_k$ respectively, given by

$$\hat{c}_k = \sqrt{G}\hat{a}_{i'_k} + \sqrt{G-1}\hat{a}^\dagger_{r_k} \tag{2.5}$$

$$\hat{d}_k = \sqrt{G}\hat{a}_{r_k} + \sqrt{G-1}\hat{a}^\dagger_{i'_k}. \tag{2.6}$$

$\hat{a}_{i'_k}$ and $\hat{a}_{r_k}$ are the creation operators of the idler and return signal modes incident at the OPA, and G is the gain of the OPA and is a function of crystal parameters and the pump power. The OPA is operated in a low-gain regime ($G = 1+\epsilon^2$) to minimize the background noise due to the interaction between the noise photons and the pump beam. Full explorations of the optimal gain and the gain of the crystal used are seen in Sec. 2.2.2 and 3.6.

When the target is present the idler modes, the return modes with noise, and the

return modes without noise are given by

$$\hat{a}_{i'_k} = \sqrt{\mu}\hat{a}_{i_k} + \sqrt{1-\mu}\hat{a}_{v_k} \tag{2.7}$$

$$\hat{a}_{r_{k_N}} = \sqrt{\kappa}\hat{a}_{s_k} + \sqrt{(1-\kappa)/\chi}\hat{a}_{b_k} \tag{2.8}$$

$$\hat{a}_{r_k} = \sqrt{\kappa}\hat{a}_{s_k} + \sqrt{(1-\kappa)}\hat{a}_{v_k} \tag{2.9}$$

$\hat{a}_{v_k}$ is the kth vacuum mode, $\hat{a}_{b_k}$ is the kth noise mode, $\hat{a}_{i_k}$ is the kth idler mode, and $\hat{a}_{s_k}$ is the kth signal mode. Thus, when a target is present, the number of photons created by the OPA per mode is $N_{1_{k_N}}$ (Eq. 2.10) if noise is present in the kth mode, and N_{1_k} (Eq. 2.11) if there are no noise photons in the kth mode.

$$\begin{aligned} N_{1_{k_N}} &= \langle \hat{c}^{\dagger}_{1_{k_N}} \hat{c}_{1_{k_N}} \rangle \\ &= G\mu N_s + (G-1)(\kappa N_s + \frac{N_b}{\chi} + 1) \pm 2\sqrt{G(G-1)\kappa\mu N_s(N_s+1)} \end{aligned} \tag{2.10}$$

$$\begin{aligned} N_{1_k} &= \langle \hat{c}^{\dagger}_{1_k} \hat{c}_{1_k} \rangle \\ &= G\mu N_s + (G-1)(\kappa N_s + 1) \pm 2\sqrt{G(G-1)\kappa\mu N_s(N_s+1)} \end{aligned} \tag{2.11}$$

Note that the $(1-\kappa)$ term does not appear in the photon per mode number. This is an artifact of the original theory paper in which the number of noise photons/mode is set to be $N_b/(1-\kappa)$ when the target is present such that there are always N_b photons per mode regardless of the presence of a target. The first terms on the right hand side of Eqs. 2.10 and 2.11 are due to the classical nonlinear interaction between the pump and idler beams. The second terms are due to the interaction between the pump and signal beams. The third terms are due to the phase correlation between the signal and idler. It is positive when the signal and idler are in phase, and negative when they are 180 degrees out of phase.

When the target is not present, the return modes with and without noise are $\hat{a}_{r_{k_N}} = \hat{a}_{b_k}$ and $\hat{a}_{r_k} = \hat{a}_{v_k}$, respectively. Thus, when there is no target present, the number of photons created by the OPA per mode k are given by Eq. 2.12 (2.13) if

noise is (is not) present in mode k.

$$N_{0_{k_N}} = \langle \hat{c}^{\dagger}_{0_{k_N}} \hat{c}_{0_{k_N}} \rangle = (G-1)(\kappa N_s + \frac{N_b}{\chi} + 1) \tag{2.12}$$

$$N_{0_k} = \langle \hat{c}^{\dagger}_{0_k} \hat{c}_{0_k} \rangle = (G-1)(\kappa N_s + 1). \tag{2.13}$$

The full output of the OPA is found by summing the contributions for all M output modes per second. To avoid confusion, N represents photons / mode while N' is photons / second.

$$\begin{aligned} N'_1 &= M\left(\chi N_{1_{k_N}} + (1-\chi)N_{1_k}\right) \\ &= M\left(G\mu N_s + (G-1)(\kappa N_s + N_b + 1) \pm 2\sqrt{G(G-1)\kappa\mu N_s(N_s+1)}\right) \end{aligned} \tag{2.14}$$

$$N'_0 = M\left(\chi N_{0_{k_N}} + (1-\chi)N_{0_k}\right) = M(G-1)(N_b+1) \tag{2.15}$$

Equations 2.14 and 2.15 show that an uneven noise spectrum is equivalent to a uniform noise spectrum as long as the average noise power is the same.

2.2.2 OPA Signal to Noise Ratio

At the output of the OPA, the signal is $N'_1 - N'_0$, the difference in the number of photons created by the OPA per second when a target is and is not present. The noise, σ'_{N_1} is the shot noise due to the probabilistic nature of photon arrival times.

$$\mathrm{SNR_{OPA}} = \left(\frac{\bar{N}'_1 - \bar{N}'_0}{\sigma_{N'_1}}\right)^2 \tag{2.16}$$

The probability mass function of the photon arrivals is given by

$$P_{N|H_m}(n|H_m) = \binom{n+M-1}{n} \frac{N_m^n}{(1+N_m)^{n+M}} \quad [6] \tag{2.17}$$

where $m = 1, 0$ if a target is, or is not present. The mean and variance of this distribution are $\bar{N}'_m = MN_m$ and $\sigma'^2_m = MN_m(N_m+1)$ [6]. Increasing the gain will increase $\bar{N}'_1$, $\bar{N}'_0$, and σ_1, thus the SNR is highly dependent on the gain of the OPA,

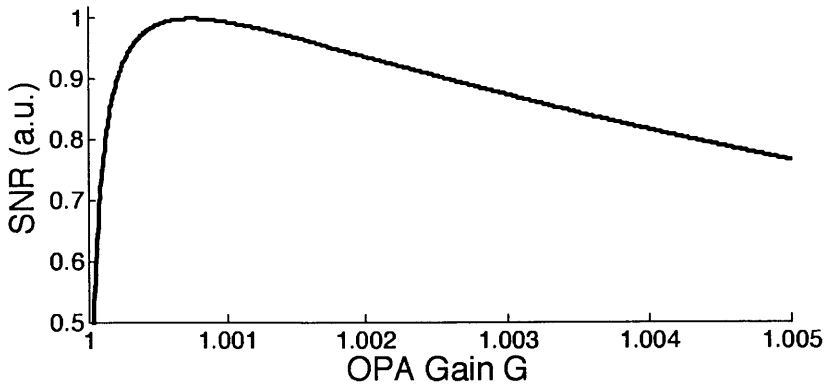

Figure 2-2: The effect of OPA gain on the signal-to-noise ratio of quantum illumination. $N_s = 0.005$, $N_b = 100$, $\mu = 1$, $\kappa = 0.1$, $M = 1.5 \times 10^{12}$.

and Fig. 2-2 shows that there is an optimal gain that is low (as suggested in Section 2.2.1). This plot has parameters $N_s = 0.005$, $N_b = 100$, $\mu = 1$, $\kappa = 0.1$. Other sets of parameters give similar shapes with shifts in magnitude and optimal gain as seen in Section 3.8. The SNR in this figure is normalized because the magnitude does not correspond to the experimental SNR. See Section 3.7 for a calculation of the expected SNR when taking the details of the full experimental setup into account.

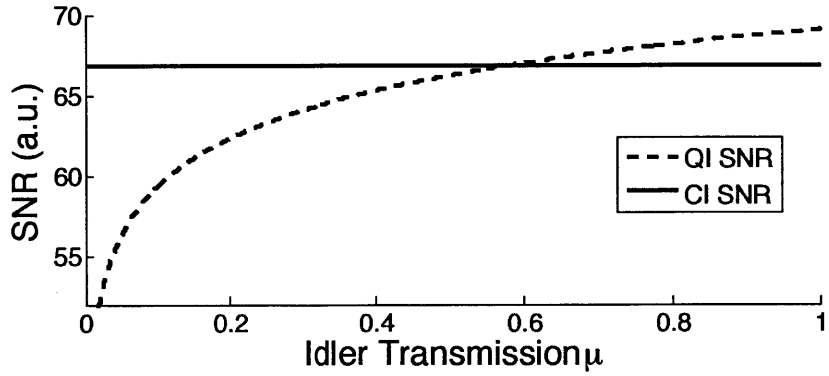

Figure 2-3: The effect of idler loss on the signal to noise ratio of quantum illumination. $N_s = 0.005$, $N_b = 100$, $\mu = 1$, $\kappa = 0.1$, $M = 1.5 \times 10^{12}$. The gain is optimized for each value of μ. The SNR of classical illumination calculated from Eq. 2.18 is shown for comparison.

Ideally, the retained idler would experience no loss. However, this is not realistic in an experimental implementation. To understand the effect of idler loss on the efficacy of quantum illumination, the SNR is plotted for different values of the amount of idler

at the OPA (μ). Each values reflects the optimal SNR for the given μ. Fig. 2-3 shows that idler loss over 40% ruins the advantage in the SNR caused by the correlation between the signal and idler. As in Fig. 2-2 the SNR is normalized.

2.3 Classical Illumination

Balanced homodyne detection provides the best signal to noise ratio at the detector when classical light is used for target detection[6]. In balanced homodyne detection, the return signal is combined with a strong local oscillator (LO) at a 50:50 beam splitter (BS). Both of the outputs of the beam splitter are monitored with balanced detectors, and the currents created by the incident photons are subtracted. The output signal will depend on the phase difference between the return signal and the local oscillator. A schematic of a simple homodyne detection system is seen in Fig. 2-4.

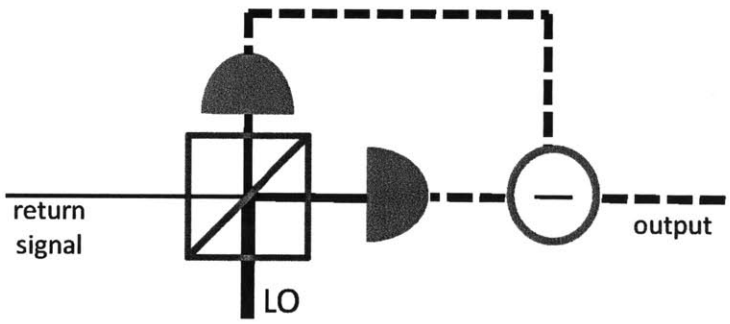

Figure 2-4: A balanced homodyne detection system.

2.3.1 Homodyne Signal to Noise Ratio

In this initial examination of the signal-to-noise ratio of target detection using classical illumination in conjunction with balanced homodyne detection, it is assumed that the detectors are perfectly balanced, shot noise limited, and have a quantum efficiency $\eta = 1$. When there is no target present, the return signal consists only of noise, as in QI. Because there is no phase coherence in the noise with respect to the LO, the

noise and LO photons incident on the BS will split evenly, and the mean output of the balanced homodyne detection system will be zero. If the target is present, the return signal will contain κN_s signal photons per mode which will have a coherent phase with respect to the local oscillator. The mean output of the balanced homodyne detection system will then be $\pm\sqrt{\kappa N_s}$—positive if the signal is in phase with the LO at the BS, and negative if the signal and LO are 180° out of phase. In both cases, the variance of the signal is dominated by the shot noise of the noise photons and is $(2N_b + 1)/4$ [6]. The LO noise is eliminated in the subtraction step of the homodyne detection [18]. The theoretical signal-to-noise ratio of classical illumination with balanced homodyne detection is then

$$\mathrm{SNR}_{CI} = \left(\frac{\sqrt{\kappa N_s}}{(2N_b + 1)/4}\right)^2. \tag{2.18}$$

Chapter 3

Experimental Implementation

Figure 3-1 shows the basic layout of the system. A high power pump beam at 783 nm of approximately 400 mW is focused into a nonlinear crystal, creating entangled photons at 1638 and 1500 nm through spontaneous parametric downconversion (SPDC) (Section 3.1). The pump is removed by a 780:1560 dichroic mirror (DM1) and the signal and idler are separated by a second dichroic mirror with a sharp cutoff at 1600nm (DM2).

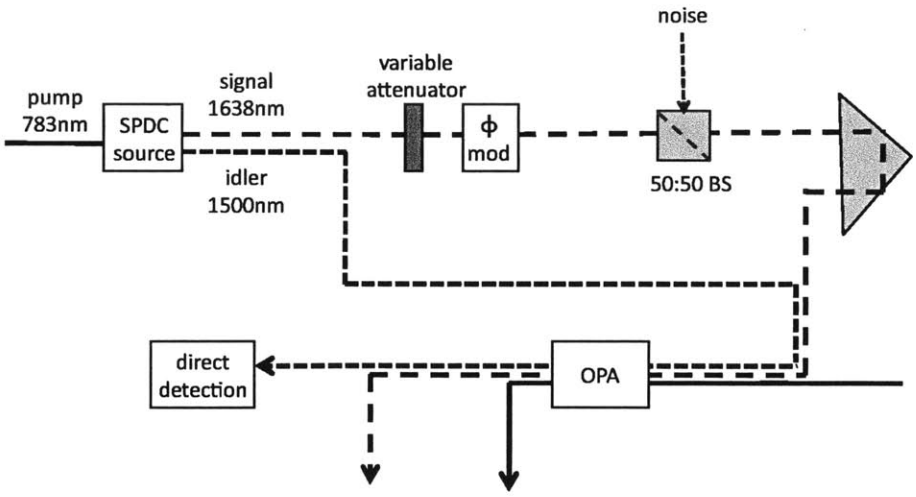

Figure 3-1: Quantum illumination setup used to produce the results presented in this thesis.

A variable attenuator is used to control the loss of the signal (Section 3.5). The remaining signal is sent through a phase modulator (Section 3.2). Noise from a

broadband diode laser at 1638 nm is added through a 50:50 beam splitter (Section 3.3). A prism mounted on a translation stage is used to adjust the signal path length (Section 3.4). The signal, idler, and pump beams are recombined with dichroic mirrors and focused into a second nonlinear crystal which forms the OPA receiver (Section 2.2, 3.6). The output of the OPA at the idler wavelength is isolated, again with dichroic mirrors, and sent to the direct detection system—an InGaAs avalanche photodiode in conjunction with a low noise transimpedance amplifier (Section 3.7). The absence (presence) of a target is simulated by blocking (opening) the signal path.

3.1 Spontaneous Parametric Downconversion

The entangled signal and idler beams are created through spontaneous parametric downcoversion (SPDC). Type-0 SPDC is used, in which the pump, signal, and idler beams are all polarized along the crystal's z axis. A periodically poled bulk lithium niobate (PPLN) crystal doped with magnesium oxide (MgO) of dimensions 40mm(x) x 1mm(z) x 3mm(y) from HC Photonics is used. In this material, the nonlinear polarization field created in response to pump photons with polarization parallel to the z axis traveling through the material under phase-matched conditions yields the signal and idler pair creation. Typical efficiencies are on the order of 10^{-10}. These signal and idler photons are entangled in time.

3.1.1 Wavelength Distribution

Conservation of energy and momentum between the absorbed pump photon, the crystal lattice, and the emitted signal and idler photons dictates the wavelengths of the emission. Energy conversion between the absorbed pump (p) photon and the emitted signal (s) and idler (i) photons ensures that $\hbar\omega_p = \hbar\omega_s + \hbar\omega_i$. The momentum mismatch between the absorbed pump photon, the crystal lattice, and the emitted

signal and idler photons is illustrated in Fig. 3-2 and given by

$$\Delta k_z = |\vec{k}_p - \vec{k}_s - \vec{k}_i - \vec{k}_{pp}| \tag{3.1}$$

$$= \frac{n(\lambda_p, T)2\pi}{\lambda_p} - \frac{n(\lambda_s, T)2\pi}{\lambda_s} - \frac{n(\lambda_i T)2\pi}{\lambda_i} - \frac{2\pi}{pT_e(T)} + \frac{n(\lambda_s, T)2\pi}{\lambda_s}\phi_s^2. \tag{3.2}$$

Equation 3.2 explicitly shows the temperature and wavelength dependence of the k vectors. The refractive indices are found using the Sellmeier equations with the coefficients for a PPLN crystal doped with MgO [9]. $\vec{k_{pp}}$ is the momentum transferred to the emitted photons by the periodic poling of the crystal. p is the poling period of the crystal and $T_e(T)$ is the crystal lattice expansion coefficient. The final term is found by assuming perfect transverse momentum matching and using the small angle approximation. The power radiated at a particular wavelength is proportional to the reduction factor $\text{sinc}^2(\Delta k_z L/2)$ [3] such that maximum power is produced when exact phase matching occurs, or $\Delta k_z = 0$.

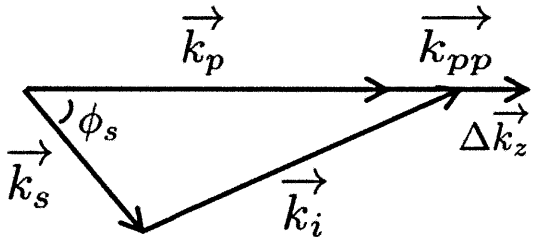

Figure 3-2: The maximum power at λ_s is emitted at perfect momentum matching between the pump, crystal, signal, and idler photons, when $\Delta k_z = 0$.

Energy conservation in concert with the momentum matching reduction factor provides a model of the spectral content of the SPDC signal. The experiment is done entirely in free space to minimize the idler loss. Thus, the difference between the signal and idler wavelengths must be large enough to split the entangled beams with low loss using a dichroic mirror (DM2). To prevent idler losses due to transmission through a dichroic mirror, the mirrors are designed to reflect the idler wavelength with a nominal reflection coefficient of 99% and transmit the signal wavelength with a nominal transmission coefficient of 95% at normal incidence. The shorter wave-

length is designated as the idler because the InGaAs photodiode used for direction detection after the OPA is more sensitive at that wavelength (Section 3.7), and it is advantageous to detect the non-signal wavelength output so the added noise can be spectrally blocked. The wavelengths are picked such that the signal wavelength matches the wavelength of the available noise source, $\lambda_s = 1638\,\text{nm}$ (Section 3.3).

Initially it is assumed that only emission collinear to the pump ($\phi_S = 0$) is produced. Figure 3-3 shows the calculated spectra of the collinear emission at two different crystal tempreatures. The solid spectrum corresponds to the signal and idler used in the experiment. The signal peak is centered at 1638 nm (FWHM, $\Delta\lambda_s = 20\,\text{nm}$) and the idler peak is centered at 1500 nm (FWHM, $\Delta\lambda_i = 17\,\text{nm}$). Because equal numbers of signal and idler photons are created in the downconversion process, and photons with longer wavelengths have less energy, less overall power is created at the signal wavelengths. The spectrum is normalized to the idler peak power.

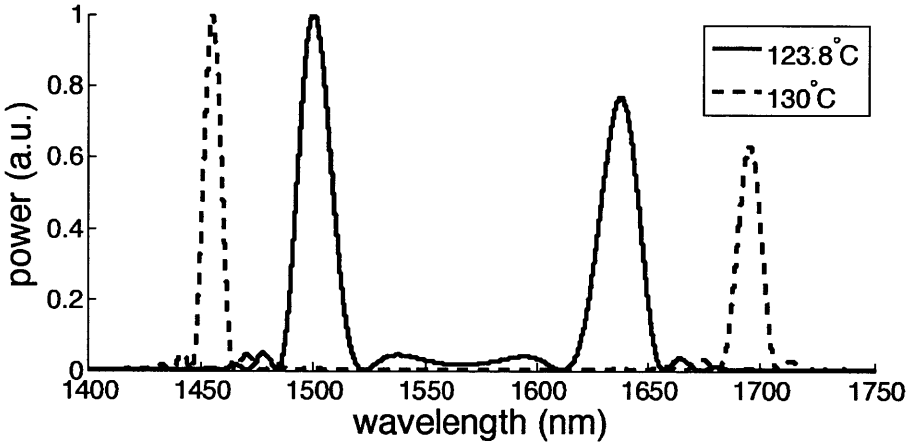

Figure 3-3: The calculated wavelength distribution of collinear emission at two temperatures.

When non-collinear emission is taken into account ($\phi_S \neq 0$), the bandwidth of the SPDC emission increases outward as seen in Fig. 3-4. Furthermore, the wavelength of the peak emission changes slightly. The dashed line in Fig. 3-4 shows the spectrum at the temperature that yields a signal peak at 1638 nm when considering only collinear emission. The solid line shows the wavelength spectrum with the temperature tuned for the non-collinear peak to be at the noise wavelength, 1638 nm. There is only a

slight difference in the spectra at the two slightly different temperatures.

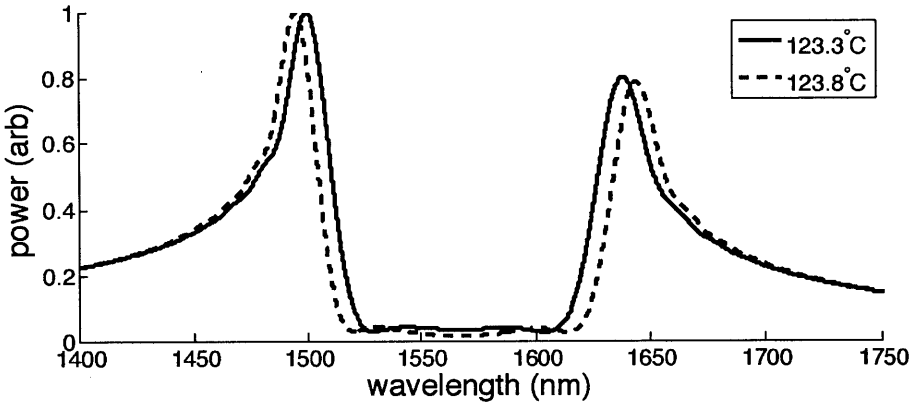

Figure 3-4: The calculated wavelength distribution of non-collinear emission at two temperatures.

The emission collinear to the pump will be mainly in the fundamental TEM_{00} mode as the pump is mainly in that mode. However, the non-collinear emission will be spread over many spatial modes. The amplification at the OPA is mediated by the pump beam, and thus power in modes orthogonal to the pump spatial mode will experience lower gain than the power in mode matching the pump modes. The bandwidth of the collinear emission is only a fraction of the full non-collinear bandwidth. Thus, only a fraction of the SPDC power will experience the maximum gain at the OPA.

3.1.2 Spatial Mode Composition

As mentioned above, the gain of the OPA is dependent on the spatial mode composition of the SPDC emission at the OPA. Although the spectral content of SPDC signals is well understood and easily modeled, the spatial structure of the entangled beams created by SPDC is much more complicated as it depends heavily on the mode composition of the pump beam. This calculation is beyond the scope of this thesis, but there have been many theoretical studies done to better understand the relationship between the focusing of the pump beam and the mode structure of the signal and idler beams. SPDC emission with high single mode content is desirable for this

experiment. Different spatial modes will suffer unequal losses during propagation, and unequal gain values at the OPA (Section 3.6). The propagation of the TEM_{00} mode is best understood, and will best match the mode of the pump at the OPA. Thus maximizing the emission in this fundamental mode is desired.

Theoretical Background

The first investigation on the effect of pump focusing on nonlinear optical interactions was done by G.D. Boyd and D.A. Kleinman in 1968 [2], soon after the first demonstration of second harmonic generation in 1961 by Franken *et al.* [4]. Boyd and Kleinman studied both parametric generation (PG) and optically resonant second harmonic generation (SHG). In PG, the output is restricted to fundamental Gaussian modes as all three beams (pump, signal, and idler) are initialized by laser beams. In optically resonant SHG, the resonator supports only Gaussian modes, and as such the output is also restricted to fundamental Gaussian modes. Restricting the mode structure to only the Gaussian modes creates tractable calculations. Boyd and Kleinman perform a rigorous theoretical examination to find the optimal pump focusing that leads to the greatest power transfer to the signal and idler beams. They introduce a focusing parameter $\zeta = L/b$ where $b = 2\pi n w_o^2/\lambda$ is the confocal parameter of the fundamental Gaussian beam and L is the length of the crystal with refractive index n. They find that the optimal situation arises when $\zeta = 2.84$, the confocal parameters of all the beams are equal ($\zeta_p = \zeta_i = \zeta_s$), and the beam waist of all three beams are at the center of the crystal [2].

A more recent theoretical study published by R. Bennink [1] extends the results found by Boyd and Kleinman to the quantum regime of SPDC where the signal and idler beams are not provided by a laser, but rather begin as vacuum modes. He assumes that the output modes of the SPDC are purely Gaussian and looks for the optimal focusing parameter to achieve maximal power in these modes. Somewhat unsurprisingly, he comes to the same conclusion as Boyd and Kleinman that a pump focusing of $\zeta_p = 2.84$ provides maximum power in the fundamental TEM_{00} mode of the entangled beams [1].

Although the seminal study by Boyd and Kleinman and the more recent Bennink paper are in perfect agreement, a more general paper published by D. Ljunggren and M. Tengner in 2005 recommends a different focusing for the pump [12]. While [2] and [1] consider only Gaussian modes, Ljunggren and Tengner provide a general analysis of the spatial makeup of the entangled light created by SPDC, assuming nothing about the content. They begin with a TEM_{00} pump described as a sum of scaled plane waves and calculate the angular distribution of the emission caused by each wave. They find that maximum single mode coupling for the SPDC emission occurs at a focusing parameter of $\zeta = 0.85$ [12]. Furthermore, they find that the focusing parameters are not the same for the pump, signal, and idler for optimal single mode coupling.

All three papers find that the efficiency of non-linear processes are extremely tolerant to changes in pump focusing. Bennink finds that a beam waist even 5 times the optimal value will reduce the peak power by only one half [1]. Ljunggren and Tengner find that the focusing is even less critical—85% of the output will couple into a single mode fiber if the focusing is within 40 times of the optimal focusing. They also observe that if $\zeta_p = \zeta_s$, the coupling efficiency will always be above 45% regardless of the pump's focusing [12].

Experimental Optimization

To better understand the effect of pump focusing on the mode composition of SPDC emission, the fraction of emission that couples into a single mode fiber is measured for different pump foci. The experimental setup is shown in Fig. 3-5. A zoom lens is incredibly useful because it allows the waist of a beam to be changed smoothly while the placement of the waist remains fixed. The simplest implementation of a zoom lens is 3 lenses—two identical convex lenses with focal length f with one concave lens in between the two with a focal length $-f/2$. In this experiment two zoom lenses are used with $f = 10$ cm to control the focus in the crystal and the mode matching to the fiber.

The zoom lens before the crystal allows the waist of the pump beam to be changed

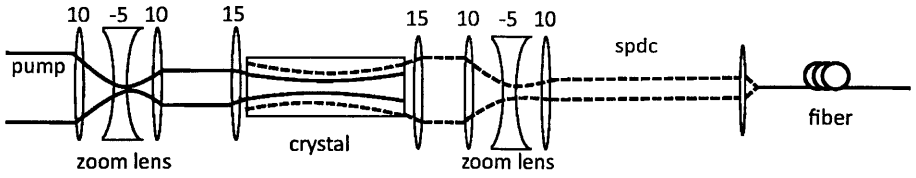

Figure 3-5: The experimental setup used to explore the effect of pump focusing on the coupling efficiency of SPDC.

in increments between 22.5μm and 33.5μm corresponding to $\zeta_p = 4.6$ and $\zeta_p = 2.1$. The first lens remains fixed while the other two lenses are translated while the beam waist is measured by placing a removable mirror before the crystal and monitoring the waist size and position with a beam scanner. There is a pair of alignment mirrors before the zoom lens to optimize the alignment into the crystal after the beam waist is changed.

The zoom lens after the crystal is used to maximize the coupling of the SPDC emission into single mode fiber. Again, the first lens in the zoom lens configuration is fixed while the other two lenses are translated while the power coupled into a single mode fiber is measured. Again, there are mirrors to optimize the alignment into the fiber.

Unlike the quantum illumination experiment, the temperature of the crystal is tuned for wavelength degenerate emission in this measurement. The focusing needed for optimal single mode coupling will change with the wavelength so a narrow band-pass filter ($\lambda_c = 1550\,\text{nm}$, FWHM $= 5.9\,\text{nm}$) is used at the emission. For each pump focusing, the power coupled into the single mode (SM) fiber is optimized with the second zoom lens. To measure the total SPDC power, the SM fiber is replaced by a multimode (MM) fiber. The alignment is then touched up and the power coupled into the MM fiber is measured. The power is measured with a fiber-coupled Agilent power meter with fW sensitivity. The number of interest is the ratio between the power coupled into the single mode fiber and that into the MM fiber. At the optimal focusing, 4 nW of SPDC are created as measured by coupling through a MM fiber with no spectral filtering. With the filter in place, 50 pW of power is coupled into the MM fiber, and 33.5 pW are coupled into the SM fiber, suggesting that 67% of the

emission within the filter bandwidth is in the fundamental mode.

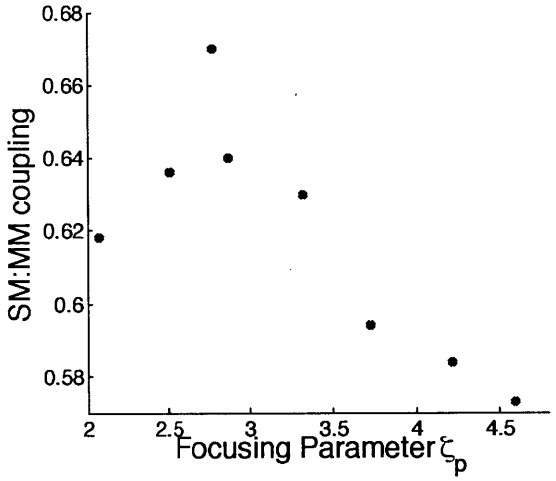

Figure 3-6: Measured ratio between power coupled into single mode and multimode fiber for varying values of ζ_p.

The data from this experiment are seen in Fig. 3-6. There is a clear peak at $\zeta_p = 2.84$ as predicted by [1, 2]. Furthermore, when the waist size of the light is traced back from the single mode fiber through the coupling lens, zoom lens, and focusing lens, it is found that the focusing parameter ζ_s of the SPDC closely matches ζ_p, matching the predictions made in [1, 2]. As expected by all the theoretical discussions, the change in coupling efficiency due to changes in the focusing parameter is slight. Because of this, the change in single mode coupling caused by misalignment of lenses could be on the order of the change in coupling efficiency seen in Fig. 3-6. Ideally, this experiment would have been repeated to establish error bars on the data taken, and the range of ζ_p would be increased. In the interest of time and because the focusing parameter is not of utmost importance in this experiment, only one set of data was taken. A focusing parameter as close as possible to 2.84 is used in this experiment into both the SPDC and OPA crystals, and the probe beams that mimic the signal and idler beams to align and mode match the system are focused such that $\zeta_p = \zeta_s = \zeta_i$. Further work should be done experimentally to verify the optimal focusing parameter in the future.

3.1.3 Crystal Characterization

Each manufactured crystal is different—the levels of MgO doping, the nonlinear coefficient d_{eff}, and the periodic poling can all differ slightly. The strength of the SPDC, the temperature needed for optimal phase matching, and the gain at the OPA depend on these characteristics and are all determined experimentally.

To characterize the crystals, a broadband laser diode is used as the probe beam. The center wavelength matches the wavelength of the signal ($\lambda_s = 1638\,\text{nm}$) and is later used to inject noise into the system (Section 3.3). The probe beam is combined with the pump beam with a dichroic mirror before the SPDC crystal. It is focused such that the probe has the same confocal parameter as the the pump as discussed in Section 3.1.2. When the pump and probe beams are present in the nonlinear crystal, difference frequency generation (DFG) will occur if the temperature is tuned to support phase matching between $\lambda_p = 738\,\text{nm}$ and $\lambda_s = 1638\,\text{nm}$ and power at the conjugate wavelength ($\lambda_i = 1500\,\text{nm}$) will be optimized (Section 3.1.1).

The beams are aligned and mode matched with the help of a beam scanner for monitoring the beam waists. The polarization of both the pump and probe are aligned to the crystal's z axis (vertical polarization). The signal and idler are separated from the pump with DM1 mirrors with a nominal transmission coefficient of 93% for the pump and a nominal reflection coefficient of 98% for the signal and idler. The idler is separated from the signal with DM2 mirrors so that the weak signal generated through DFG can be measured out of the strong background of the probe beam. The power at the idler wavelength is coupled into a multimode fiber. The temperature of the crystal is varied until the power coupled into the fiber is maximized. The temperature at which the probe wavelength (1638 nm) is phase matched with the pump beam will also support SPDC output at the 1638 nm due to phase matching. The optimal temperature is found to be 134.0°C for the SPDC crystal. The alignment of the probe is tuned to maximize the DFG power—this ensures that the probe beam will follow the path of the signal and idler through the system and so can be effectively used to align the remainder of the system.

The DFG power created in a crystal is given by [11]

$$P_i = \left[\frac{16\pi d_{\text{eff}}^2 l \bar{h}_m(B,\zeta)}{c\epsilon_0 n_p n_s n_i \lambda_i^2 (1/k_s + 1/k_p)}\right] P_p P_s \quad . \tag{3.3}$$

where $\bar{h}_m(B,\zeta)$ is the reduction factor due to beam walk off and can be approximated to 1.068 for a focusing parameter $\zeta = 2.84$ [3]. The generated idler power is measured for various pump powers. For all measurements, 5.5 mW of V-polarized probe light

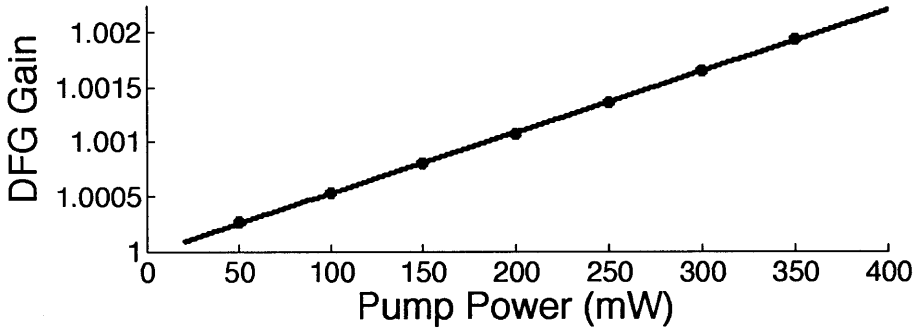

Figure 3-7: Measured SPDC crystal gain.

is used. The nonlinear gain of the crystal is the quantity of interest and is given by $G = 1 + P_i/P_s$ where P_i is the amount of DFG power created, and P_s is the amount of probe power used. The data for the measurement are plotted in Fig. 3-7. A line is fit to the data to estimate the nonlinear coefficient of the crystal d_{eff} through the linear relationship of Eqn. 3.3. It is found that $d_{\text{eff}} = 8.3\,\text{pm/V}$. This number is significantly lower than the expected value of approximately 13 pm/V. This is due to the broadband emission of the diode laser used (see Section 3.3 for the measured spectrum).The entire power output of the laser is not perfectly phase matched, and thus the effective probe power is much less than the total measured probe power, increasing d_{eff}.

3.1.4 Emission Characterization

It is important to understand the actual spectral and spatial composition of the emission created through SPDC. It is assumed that the SPDC and OPA crystals

create spatially and spectrally equivalent emission profiles when tuned to the correct temperatures.

To understand the spectral content of the emission an interference filter with a pass band that is slightly smaller than the collinear bandwidth is used ($\lambda_c = 1639.2\,\text{nm}$, $\Delta\lambda_{\text{FWHM}} = 18\,\text{nm}$, $T_p = 77\%$ Andover Corp.). From the transmission information provided, the filter is approximated by a Gaussian $T(\lambda) = A\exp(-\frac{(\lambda-\lambda_c)^2}{\lambda_{FWHM}/4\ln 2})$, ehere A is chosen such that the maximum value is T_p. This approximated transmission spectrum is shown in Fig. 3-8.

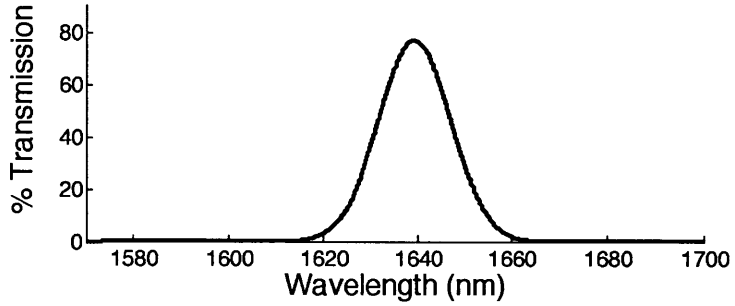

Figure 3-8: The approximate transmission spectrum of the interference filter ($\lambda_c = 1639.2\,\text{nm}$, $\Delta\lambda_{\text{FWHM}} = 18\,\text{nm}$, $T_p = 77\%$ Andover Corp.).

The OPA is pumped with 300 mW of 783 nm pump power. The signal is isolated from the idler by placing a DM2 mirror in the path, reflecting all idler photons. The signal power is focused onto the detection system (Section 3.7) in free space to avoid any issues of coupling the multi-mode emission into fiber. The responsivity of the InGaAs APD detector (Sec. 3.7) drops off precipitously above 1600 nm, so a measurement of the full signal bandwidth would be imprecise. Thus, the power of the full idler bandwidth is measured and used to determine the signal power through $P_s = P_i\lambda_i/\lambda_s$. Through this, it is found that 5.1 nW of signal power is created. The responsivity of the APD within the filter bandwidth is assumed to be constant at 0.8 A/W. It is found that only 1 nW of signal power remains when the filter is placed in the path. Taking the transmission of the filter into account, it is calculated that only approximately 20% of the SPDC emission is within that bandwidth. This fits well with the expected transmission through the filter of the full non-collinear spectrum

calculated in Section 3.1.1.

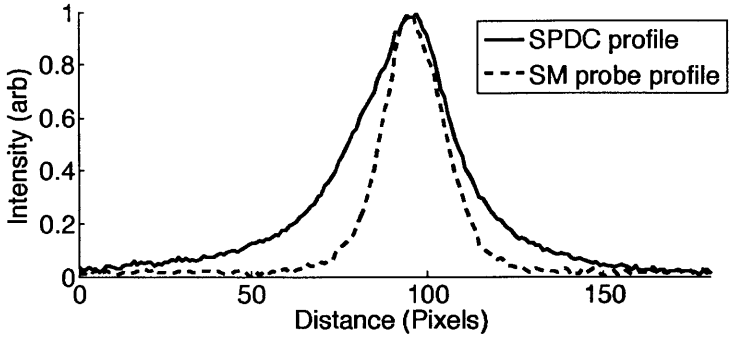

Figure 3-9: A comparison between the measured cross-sectional beam profiles of the multi-mode SPDC emission at the idler wavelength and a single mode (SM) probe beam.

Measurements of the spatial mode composition of the SPDC emission supports the claim that a majority of the emitted power is non-collinear. An extremely sensitive InGaAs CCD camera is used to capture images of the SPDC emission. The shape and size of the SPDC emission is compared with that of a probe beam attenuated to have the same peak power. Figure 3-9 shows that the SPDC emission has a much larger spatial extent than the single mode probe beam, suggesting that there is considerable emission outside of the fundamental Gaussian mode.

3.2 Phase Modulation

The power created in the OPA due to the correlation between the signal and idler is extremely small compared to the power due to the nonlinear interaction between the pump and the noise photons at the OPA. As shown in Section 2.2.1, the OPA creates N_1' photons per second at the idler wavelength,

$$N_1' = \left(G\mu N_s + (G-1)(\kappa N_s + N_b + 1) \pm 2\sqrt{G(G-1)\kappa\mu N_s(N_s+1)}\right) M \qquad (3.4)$$

To distinguish the phase-dependent amplification of the third term from the phase-independent background of the first two terms, the signal's phase is modulated. An analysis of the frequency spectrum of the received signal will then reveal a sharp

peak at the modulation frequency if a target is present due to the phase sensitive interaction between the entangled signal and idler. If no target is present, there will be no peak. Thus the measured SNR will be slightly modified from the SNR of Eqn. 2.16 to

$$\begin{aligned} \mathrm{SNR}_{\mathrm{opa}} &= \left(\frac{2N'_{1AC}}{\sigma_{N'_1}}\right)^2 \\ &= \frac{16\,G\,(G-1)\,\kappa\,\mu\,N_s\,(N_s+1)}{\sigma^2_{N'_1}} \end{aligned} \tag{3.5}$$

The phase is modulated with an electro-optic broadband phase modulator (New Focus Model 4004) consisting of a MgO-doped lithium niobate crystal. A strong modulated electric field E is applied to this crystal with a high voltage amplifier (New Focus Model 3211). This induces a change in the crystal's refractive index given by $\Delta n = 1/2 n_e^2 r_{33} E$. The beam must be aligned to clear the 2 mm input and output apertures. For optimal operation, the Rayleigh range of the light should be larger than the length of the crystal. In this setup, the beam is collimated with a beam diameter of approximately 450 μm. No further focusing is done on the signal arm before the lens used to focus the signal and idler into the OPA crystal.

The crystal is birefringent and thus the light must be polarized vertically with respect to the crystal's z axis. If the polarization is not matched precisely, the modulator will impose a polarization rotation on the non-vertical component of the light. The first two terms in Eq. 3.4 are not phase sensitive, but they are polarization sensitive. Therefore, a polarization modulation on the signal will create an amplitude modulation at the output of the OPA due to the first two terms. If that is the case, modulation will be seen even if no target is present, increasing the probability of error. Thus, it is extremely important that the polarization matches the crystal axis precisely. There is a PBS directly before the phase modulator used to control the loss experienced by the signal (Section 3.5) and thus all light incident on the phase modulator is vertically polarized with respect to the PBS. However, the plane of the crystal and the plane of the PBS may not match. To ensure polarization matching, a HWP is placed at the input of the phase modulator. The necessary rotation is

determined by applying a modulating field to the crystal and monitoring the output port of a PBS after the phase modulator. The polarization alignment is correct when there is no amplitude modulation for any input polarization to the test PBS.

At the OPA, the pump, signal, and idler fields are given by $|E_p|e^{i\phi_p(t)}$, $|E_s|e^{i\phi_s(t)}$, and $|E_i|e^{i\phi_i(t)}$. The amplitude of the power due to signal-idler entanglement is thus proportional to $e^{i(\phi_p-\phi_i-\phi_s)}$ and is maximized when $\phi_i+\phi_s=\phi_p$ and minimized when $\phi_i+\phi_s=\phi_p\pm\pi$ [10]. The modulation offset and amplitude necessary to create a full π phase shift is found by measuring the modulation depth of the classical interference between two probe beams. Initially, the modulation amplitude is set to be much smaller than the ideal amplitude and the offset is changed to find the optimal offset. Then the amplitude is increased until the modulation depth of the classical interference is maximized. This was done with probe beams at 1550 nm. The voltage $V_\pi=\frac{\lambda d}{n_e^3 r_{33} l}$ needed to create a full π shift is linearly dependent on the wavelength, so the voltage necessary for the signal wavelength, 1638 nm is easily found. The expected amplitude and modulation is confirmed with the signal peak created at the OPA. The final modulation amplitude was 224 V_{pp} with an offset of -25 V.

The modulation function $m(t)$ imposed on the signal phase by the modulator determines the frequency spectrum of the amplitude at the output of the OPA. A sinusoidal modulation of the phase creates an amplitude proportional to $e^{\beta\sin(\omega t)}=\sum J_k(\beta)e^{ik\omega t}=J_0\beta+J_1\beta 2i\sin(\omega t)+J_2(\beta)2\cos(2\omega t)+.....$ This is not an ideal modulation pattern as the power is split between many frequencies. Worse, significant power is lost to a DC component which will not be detectable over the background noise. Furthermore, odd multiples of the fundamental frequency ω are orthogonal to even multiples making it difficult to maximize the full amplitude. A square wave modulation provides more power concentrated at the fundamental frequency, and none is lost to a DC component. Furthermore, the amplitude of all harmonics are in phase. A comparison of the two power spectral densities expected from sinusoidal and square wave inputs are shown in Fig. 3-10.

The amplitude of the fundamental frequency does not translate exactly to the full peak-to-peak modulation of the signal. The modulation power is split between multi-

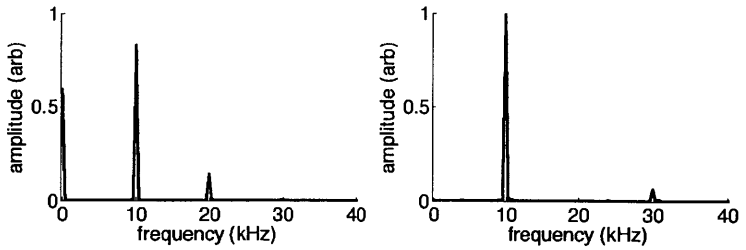

Figure 3-10: Calculated power spectrum density due to sinusoidal (left) and square (right) wave phase modulations.

ple frequencies and the windowing function used by the spectrum analyzer can affect the amplitude. The conversion factor is found by performing classical interference and modulating the phase of the signal with a square-wave modulation to create an amplitude modulation with the same spectral distribution but a larger amplitude for ease of measurement on an oscilliscope. The peak-to-peak depth is measured on an oscilliscope and compared to the peak on the spectrum analyzer—it is found that the peak voltage on the spectrum analyzer must be multiplied by 4 to match the actual V_{pp} of a square-wave modulation.

Unfortunately, the phases of the idler and signal are not stable due to air turbulence and path length fluctuations. Their phases will fluctuate around their mean values. This phase instability causes the height of the spectral peaks to vary due to the changes in the relative phase. However, by tracking the peak of the amplitude modulation on the spectrum analyzer, the maximum value can be found within seconds. In principle, the peak could also be obtained by slowly sweeping the phase of the signal using a piezoelectric transducer attached to a mirror located within the path of the signal.

3.3 Noise

Quantum illumination provides an advantage over classical illumination in target detection because it provides better distinction between noise photons and signal photons. The correlation between the idler and the returning signal due to prior

entanglement is stronger than any classical-state transmitter would obtain for the same amount of loss and noise. This reduces the probability of incorrectly concluding that a target is present when noise photons are incident on the detection system.

The theory presented in Section 2.1 assumes a uniform level of noise across the SPDC bandwidth. An incandescent light has strong thermal emission in the infrared range and a uniform power level across the bandwidth of interest, making it the ideal noise source. Ideally the incandescent light would be coupled into a single mode fiber, and then mode matched to the signal to ensure the correct number of photons per mode. Unfortunately, an incandescent source emits light over the full 4π solid angle, and thus it is difficult to couple enough optical power into a single mode fiber within the desired bandwidth. Instead, a broadband diode laser is used with a center wavelength of 1638 nm and a FWHM of 8 nm and a total output power of 12 mW (ThorLabs FPL1059S). Unfortunately, this diode laser does not provide the flat thermal noise spectrum expected by the theory as seen in Fig. 3-11. The effect of this uneven power density spectrum is discussed in Section 2.2.1, and Eqs. 2.14, 2.15 make it clear that the exact shape of the spectrum of the noise source within the bandwidth of interest is not important. Only the average noise photons per mode within the signal bandwidth matters.

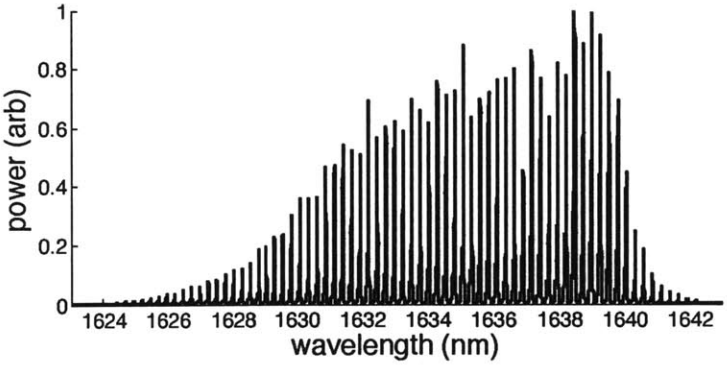

Figure 3-11: The measured wavelength distribution of the 1638nm diode laser used as a broadband noise source.

The noise is injected into the signal path through a 50:50 beam splitter after the signal is phase modulated. It is carefully aligned and mode matched with the

signal and pump beams. This is confirmed through classical interference and DFG respectively. To estimate the amount of power needed to achieve 100 photons per mode, the collinear bandwidth calculated in Section 3.1.1 is used to calculate the number of temporal modes per second through

$$\Delta f_{\text{FWHM}} = \frac{c}{\lambda^2}\Delta\lambda_{\text{FWHM}} \tag{3.6}$$

where Δf is the FWHM of the frequency distribution and $\Delta\lambda$ is the FWHM of the spectral distribution. A signal bandwidth (FWHM) of 20 nm gives $M = 2.2 \times 10^{12}$ modes per second, or a necessary noise power of 26 μW to achieve an average of 100 photons per mode. The diode laser is always run at 200 mA because the wavelength distribution is dependent on the current. The power injected into the system is controlled through a fiber coupled attenuator. The loss at the beam splitter and subsequent optical elements is taken into account when setting the power. As dictated by the theory, there are always N_b photons per mode at the OPA regardless of the presence of a target.

3.4 Path Matching

Quantum illumination depends upon the interaction between a pair of entangled photons, so it is essential that the entangled signal and idler photons arrive at the OPA at the same time. The temporal bandwidth of the emission is related to the frequency bandwidth through Eq. 3.6. It is assumed that the entanglement temporal envelope is Gaussian-shaped, giving a time-bandwidth product of

$$\Delta f \Delta t = \frac{2\ln 2}{\pi}. \tag{3.7}$$

The expected envelope width is estimated by assuming that the spectral bandwidth of the entanglement matches the collinear bandwidth calculated in Section 3.1.1 - $\Delta\lambda_{s_{\text{FWHM}}} = 20\,\text{nm}$, $\Delta\lambda_{i_{\text{FWHM}}} = 17\,\text{nm}$. Thus, the FWHM temporal bandwidth of this system is expected to be approximately 0.2 ps, giving a coherence length FWHM of

60 μm.

Initial path length matching is done by hand, taking into account the refractive indices of all optical elements that the light passes through. It is impossible to match the length of the signal and idler within 60 μm in this way, so a prism is placed in the signal path on a translation stage with μm precision to tune the length of the signal path without changing the alignment. The length of the two arms are matched as closely as possible, taking into account the refractive indices of all optical elements that the light passes through.

A bit error rate tester is used to create a square amplitude modulation with fast rise time. This amplitude modulation is imposed on two probe beams simulating the signal and idler beams. One is at 1638 nm and follows the signal path. The second is at 1524 nm—the closest available to the idler wavelength—and follows the idler path. For each path, the 1/2 magnitude position of the rise time is measured as accurately as possible. Taking the 17 ps/nm/km dispersion through fiber into account, the prism is translated to align the pulses. Unfortunately, the power through the system—especially for the idler path—is not large, and so the resolution of this method is only about 0.5 ps, or 150 μm which is still above the 60 μm needed to ensure exact path matching. The path length is finalized while looking at the actual QI signal created by the OPA.

3.4.1 Bandwidth Measurement

To experimentally determine the coherence time, and thus the optical bandwidth of the SPDC emission, the power of the modulated phase-sensitive signal out of the OPA is measured as the path matching is detuned by translating the prism. As the prism is translated, the signal pulse is scanned over the idler pulse. The power created by the OPA will be maximized when the signal and idler pulses are fully overlapped. The power will decrease as less of the entanglement pulses overlap. This effect is seen in Fig. 3-12. As mentioned above, it is assumed that the entangled fields have a Gaussian-shaped temporal amplitude envelope given by $T_E(t) \propto e^{-\frac{t^2}{2\Delta t^2}}$ or in space, $T_E(z) \propto e^{-\frac{z^2}{2\Delta z^2}}$ where Δz is the standard deviation of the envelope. These envelopes

will be the same for the signal and idler fields. When the signal is detuned a distance z_r from complete overlap with the idler field at z_0, the reduction factor is given by

$$\begin{aligned} R(z_r) &= \int dz\, T_E(z - z_0)\, T_E(z - z_0 - z_r) \\ &= \int dz\, e^{-\frac{(z-z_0)^2}{2\Delta z^2}} e^{-\frac{(z-z_0-z_r)^2}{2\Delta z^2}}. \end{aligned} \tag{3.8}$$

A least squares optimization is used to fit a numerical evaluation of Eq. 3.8 to the measured data with Δz and z_0 as free parameters. This fit suggests that $\Delta z = 55\,\mu$m with an R^2 correlation coefficient of 0.97. For a Gaussian distribution, the FWHM is related to the standard deviation through

$$\Delta z_{\text{FWHM}} = 2\sqrt{\ln 2}\Delta z. \tag{3.9}$$

Using Eqs. 3.9, 3.7, and 3.6 the expected FWHM of the signal and idler spectral distributions are $\Delta\lambda_s = 13\,$nm and $\Delta\lambda_i = 10.86\,$nm. These measured bandwidths are similar, though slightly smaller, than the FWHM values calculated from the spectral bandwidth of the collinear emission in Section 3.1.1. The fact that this calculated interaction bandwidth closely matches the collinear bandwidth, and not the bandwidth of the full non-collinear emission suggests is consistent with the belief stated in Section 3.1.1 that the non-collinear emission will experience lower gain at the OPA than the emission that is collinear with the pump beam.

The number of temporal modes per second is approximated by the FWHM of the frequency distribution ($M = 1.45 \times 10^{12}$) from the assumption that temporal modes only have a significant contribution if they have greater than 50% transmisstivity.

3.5 Loss

As the signal travels from the transmitter, to the target region, and finally to the receiver it is assumed to experience a high level of loss. There is some loss inherent in the optical setup. The loss from when the signal and idler are separated with a

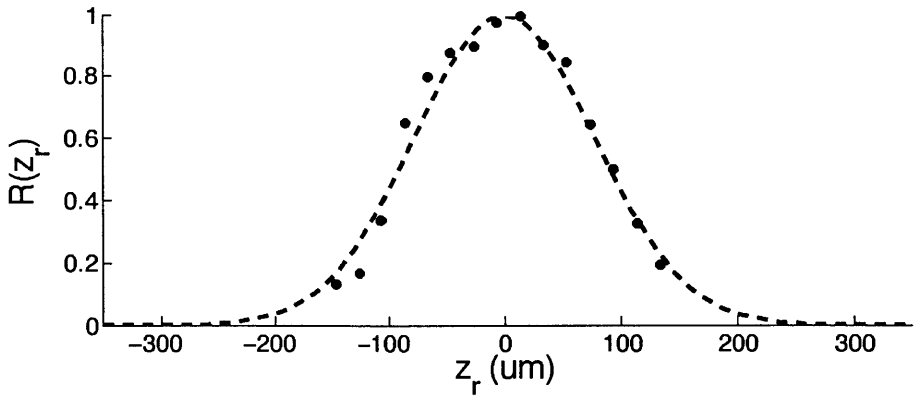

Figure 3-12: Measured power decrease as the path lengths are detuned by z_r, twice the translation of the prism. The data are fit to Eqn. 3.8 with a least squares optimization.

sharp dichroic mirror (DM2) to their recombination with a second DM2 is estimated by measuring a probe beam at the signal wavelength at each step of the setup. After the recombination, approximately 25% of the signal remains. The breakdown of loss due to transmission through the setup is shown below.

Element	% Loss
4 DM1	6.3
DM2	5.5
Phase Modulator	15.4
50:50 BS	50
Prism	18.3
DM2	5.8

The most loss occurs at the 50:50 beam splitter where the noise is injected, as expected. There is also significant loss through the phase modulator and the prism. There is slightly more loss through the second dichroic mirror because it is sent through the back of the dichroic mirror, meaning that it experiences slightly different coating conditions. Multiplying the percents retained gives the total power retained through the system, $\kappa_0 = .25$. A half wave plate is placed in front of the PBS at the phase modulator input to control the overall system transmission κ by increasing the loss.

Ideally, there should be no loss in the idler pathway. To minimize this loss the fewest possible optical elements are used in the idler pathway. Of course, mirrors are necessary for path alignment, and lenses are necessary for mode matching, but only two of each element are used as well as the two DM2s to separate and recombine the signal and idler beams. To measure the loss, strong pump and probe powers are sent through the SPDC to create μW levels of DFG power which is then measured through the system.

With this setup, only 20% of the idler is lost. The majority of this loss occurs at the dichroic mirrors and is due to non—0° incidence. The incidence angles are minimized but there is still loss. The effect of idler loss on the SNR of QI is discussed in Section 2.2.2 where it is found that if only 60% of the idler is present at the OPA, the quantum advantage of QI will be lost, and the signal to noise ratio will match that of the classical case.

3.6 Optical Parametric Amplification

A periodically poled bulk MgO-doped lithium niobate (PPLN) crystal similar to the crystal for SPDC is used (Sec. 3.1). It has the same dimensions: 40mm(x) x 1mm(y) x 3mm(z). The temperature of this crystal is tuned for maximum phase matching between the pump, signal, and idler beams. As discussed in Section 2.2.1, power is created at the signal and idler wavelengths due to nonlinear interactions with the crystal.

3.6.1 Mode Matching

The alignment and mode matching of the pump, signal, idler, and noise beams is extremely important to ensure maximum gain at the OPA. As discussed in Section 3.1.2, the beams are focused such that $\zeta_p = \zeta_s = \zeta_n = \zeta_i = 2.84$ for optimal power transfer between beams. There are many constraints on the alignment and mode matching of the beams, and the setup used to do this at the OPA is shown in Fig. 3-13.

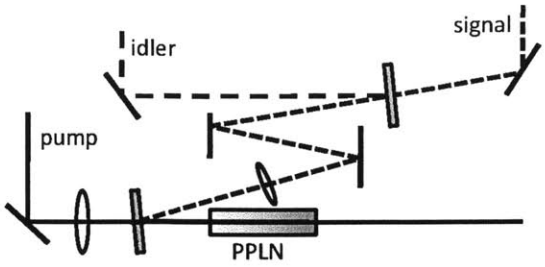

Figure 3-13: Alignment and focusing into the OPA crystal.

To minimize losses due to the dichroic mirrors, the beams must have near 0° incidence. To minimize losses due to optical elements anti-reflection coated at the wrong wavelengths (e.g. pump loss due to transmission through a lens coated for 1560 nm and vice versa), all focusing and alignment is done before the pump and signal/idler beams are combined.

The signal, idler, and pump are all approximately collimated after the SPDC crystal. As mentioned in Section 3.2, the signal is re-collimated to have a beam waist of 225 μm as required by the phase modulator. Due to the small waist size, there is still considerable beam expansion from the phase modulator to the OPA. In fact, this is advantageous because it allows tight focusing into the crystal with a lens with a large focal length which is necessary as seen in Fig. 3-13 due to the constrains mentioned above.

The idler is re-collimated to match the beam waist size and position of the signal. The mode matching and alignment is verified by sending a probe beam through the idler path at 1524 nm, and a second probe through the signal path 1648 nm. The beam sizes and waist position are matched using a beam scanner. The pump and noise are mode matched in the same way. The final lens which focuses the signal, noise, and idler beams into the OPA crystal has a focal length of 12.5 cm. At this lens, the beam waist of the signal (idler) is 1.6 mm (1.5 mm). Both the signal and idler beams are focused down to a waist of 33 μm located 11.3 cm after the $f = 12.5$ cm lens. The pump beam is focused down to 30 μm.

This process of mode matching is unfortunately prone to error because the beam

scanner has only μm resolution. Furthermore, the focusing of the actual signal and idler created through SPDC will not match that of the probes used, due to the complicated spatial mode of the SPDC emission as discussed in Section 3.1.2.

The signal and idler beams are aligned by sending a probe at 1554 nm through the system. At that wavelength, the power from the signal and idler paths are equal, and classical interference will occur. The alignment is tweaked to maximize the interference depth. The signal/idler path and the noise path are aligned with the pump by maximizing DFG through the OPA crystal.

3.6.2 OPA Efficiency

DFG is used to characterize the crystal as explained with the SPDC crystal in Section 3.1.3. The gain of the crystal as measured through DFG depends on the alignment and mode matching of the pump and probe beam. Because the signal and noise paths are aligned and mode matched separately, the gain is measured in both cases. The data from these measurements are shown in Fig. 3-14 a. The nonlinear crystal gain is also measured with a constant pump power of 400 mW, while changing the amount that is vertically polarized. As in the SPDC crystal, there is little difference between these cases and thus the data are not shown.

Fig. 3-14 a shows that for a given pump power, the gain is slightly lower for the signal path than the noise path. For the signal and idler, $d_{\text{eff}} = 8.3\,\text{pm/V}$. For the noise beam, $d_{\text{eff}} = 9.4\,\text{pm/V}$. This difference is most likely due to slightly better mode matching between the noise and the pump as compared to the mode matching between the signal and the pump. As noted in the characterization of the SPDC crystal, these d_{eff} values are lower than expected due to the broad spectrum of the probe laser used.

This difference in gain between the signal and noise is important when interpreting the results (Section 4). The noise will be amplified more strongly than the signal, leading to a lower SNR. Starting from the SNR of Eqn. 3.5, it is assumed that $\sigma^2_{N_1'}$ is dominated by the emission created by the noise photons as $N_b \gg N_s$. To take the lower signal gain into account, the SNR is scaled by $\frac{G_{si}(G_{si}-1)}{G_n(G_n-1)}$. The calculated

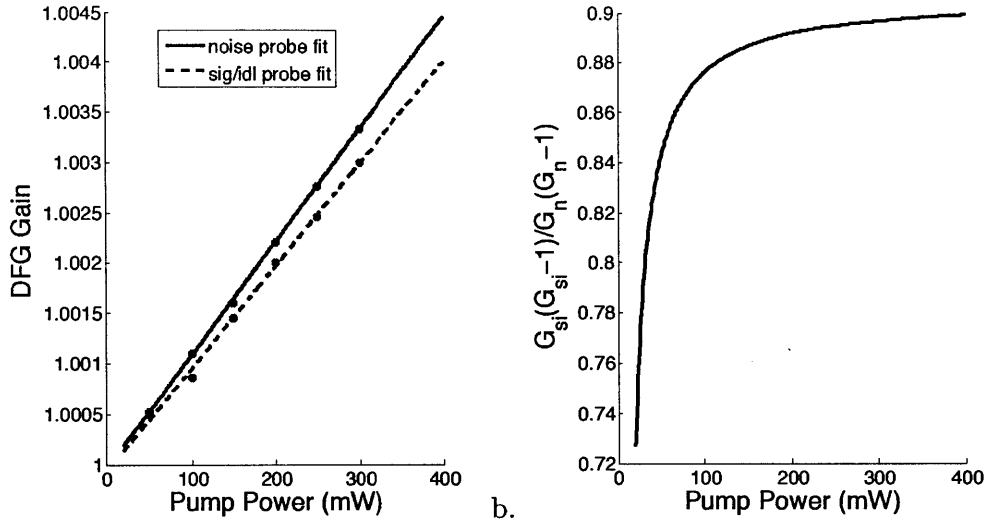

Figure 3-14: a. Measured OPA crystal gain for different pump powers. b. Calculated reduction coefficient due to the difference of the OPA gain with the noise or signal beams.

ratio as it depends on the pump power is plotted in Fig. 3-14b and shows that this mismatch has a non-negligble effect, especially for low pump powers.

3.7 Direct Detection

The output of the OPA is filtered to eliminate the pump (four bounces off a DM1) as well as the signal (four bounces off a DM2). The power at the idler wavelength is then detected by an indium gallium arsenide (InGaAs) avalanche photodiode (APD) (GPD optoelectronics IAV80) which has a responsivity of 1 A/W at the idler wavelength and 0.8 A/W at the signal wavelength. The current created by the APD is amplified through an ultra-low-noise current amplifier (Femto LCA-100K-50M). In this section, the noise contribution of each element is discussed and the expected signal-to-noise ratio of the voltage output under QI is calculated.

3.7.1 Current Amplifier

The transimpedance amplifier has a gain of $R_f = 5 \times 10^6$ V/A and extremely low noise, allowing it to be shot noise limited at the powers detected in this experiment.

It has a maximum measurement bandwidth of 100 kHz. The phase modulation is done at 16 kHz, well within the measurement bandwidth. There are three sources of electronic noise inherent in the detector—voltage noise, current noise, and thermal noise. The input noise current is 30 fA/$\sqrt{\text{Hz}}$, or 1.5μV/$\sqrt{\text{Hz}}$ at the output. The input noise voltage is V_n = 5nV/$\sqrt{\text{Hz}}$. The output noise due to the input voltage noise is $V_n \frac{R_f}{R_s}$ = 60 pV/$\sqrt{\text{Hz}}$ where $R_s = 4.2 \times 10^{11}$ is the impedance of the APD and is dependent on the capacitance of the detector (0.38pF) and the measurement bandwidth. The thermal, or Johnson noise is $V_j = 0.9\mu\text{V}/\sqrt{\text{Hz}}$ at room temperature.

To verify this, the noise spectrum is measured with a FFT Network Analyzer (Stanford Research Systems Model SR770). All measurements are done with the power spectral density setting as this accounts for both the measurement bandwidth and the windowing function used. To determine the noise floor, 500 measurements are averaged.

The network analyzer has a noise floor of 99.5 nV/$\sqrt{\text{Hz}}$. The noise floor of the amplifier when a 50Ω terminator is at the input is 0.955μV/$\sqrt{\text{Hz}}$, reflecting the johnson noise as the input noise current is grounded due to the terminator. When the APD detector is connected without bias voltage or optical input, the noise floor is measured to be 2.8μV/$\sqrt{\text{Hz}}$, close to the 2.4μV/$\sqrt{\text{Hz}}$ expected from the specifications of the amplifier.

3.7.2 InGaAs APD

Avalanche photodiodes are able to detect extremely small optical signals. A high reverse bias voltage is applied which creates a large electric field across the InGaAs detector. As an electron is freed by an incident photon, it accelerates quickly in the field and creates an "avalanche" of other free electrons through impact ionization. Thus the small optical signal is amplified even before it reaches the external current amplifier.

Of course this amplification does not come without a cost. Increasing the voltage bias will increase the number of electrons freed with each incident photon, or the gain M_{apd}. However, the dark current will also increase. The dark current $I_D$is composed

of a surface leakage current I_{DS} and a bulk leakage current I_{DB} which is multiplied by M_{apd}. $M_{\text{apd}} I_{DB} \gg I_{DS}$, so I_{DS} is neglected when calculating the expected shot noise.

Furthermore, APDs generate excess noise due to the statistical nature of the avalanche process—the hole and electron ionization probabilities are not equal. This excess noise factor, F is dependent on the APD gain M_{apd} and the effective ratio between the hole and electron ionization rates, k_{eff} through the McIntyre model [14]. This noise factor increases the shot noise and for a given signal power P_s at a wavelength with an APD responsivity of R and a measurement bandwidth of B, the shot noise is given by Eq. 3.10 show that an APD creates a shot noise level $\sqrt{F}$ higher than the shot noise of a standard photodiode detector.

$$I_{sh} = \sqrt{2q(I_{DB} + RP_s)FB}\, M_{\text{apd}}\,. \tag{3.10}$$

The responsivity of the InGaAs APD is approximately 1A/W at the idler wavelength 1500 nm and at the wavelength used to characterize the detector, 1550 nm. Due to the tradeoff between APD gain and dark current, there is an optimal bias voltage which maximizes the SNR of the output. To find this bias voltage, an optical power of 3 nW is focused onto the active area of the APD and the output DC voltage V_3, dark voltage V_0, and the total noise level σ_T, and the detector noise level without light input σ_0 are measured as the bias is increased. The APD gain is calculated as $\text{M}_{\text{apd}} = \frac{V_3 - V_{\text{dark}}}{5\times10^7 3\times10^{-9}}$. The SNR of the output is given by

$$\text{SNR}_{\text{apd}} = 10\log_{10}\frac{(V_3 - V_0)^2}{\sigma_T^2} \tag{3.11}$$

The results of these measurements are seen in Fig. 3-15. It is found that the optimal bias is 50V, which corresponds to a gain of $M_{apd} = 3.68$ and dark current of $I_d = 1.74$ nA. The low gain is advantageous because the current amplifier has a maximum input current of 200 nA—with high levels of noise ($N_b = 100$) the current created by the APD at a higher gain, would saturate the amplifier. Because of the low

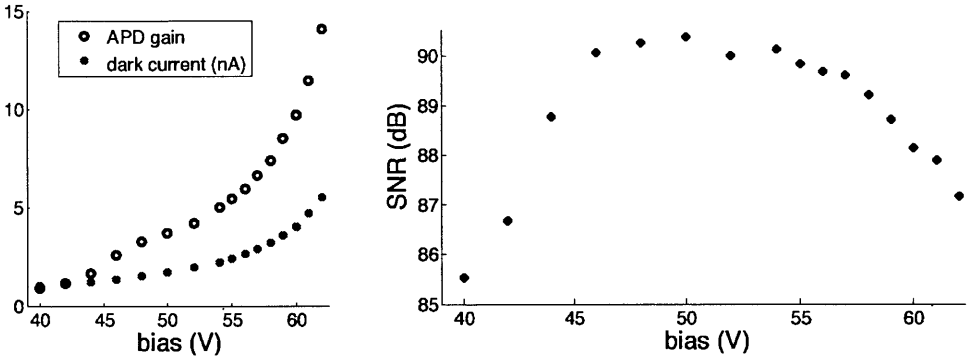

Figure 3-15: The effect of a bias voltage on a.) the dark current and gain of the APD. b.) the SNR with 3nW optical power input.

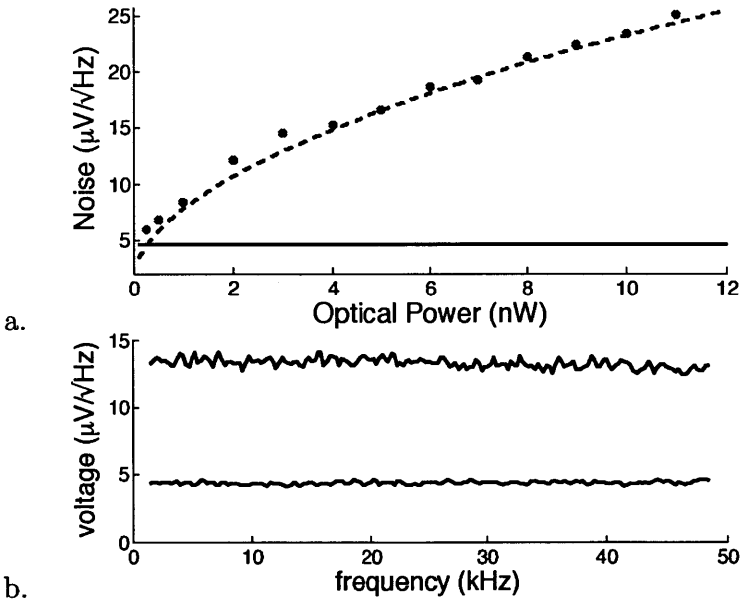

Figure 3-16: a. Measured shot noise at various optical powers fit to Eqn. 3-16 with a least squares optimization to determine F. The dark noise level is shown for comparison. b. Noise floor with no optical input and 3 nW optical power input—averaged over 500 measurements, normalized to $/\sqrt{\text{Hz}}$.

noise of the amplifier, the detection system is nearly shot noise limited at an optical power of 3 nW. It is confirmed that the laser is shot noise limited at the measurement frequency (16 kHz) by measuring the DC and noise levels on a standard photodiode detector (Thorlabs PDA400) and comparing them to the expected levels. With an optical input of 5 μW, the noise level was 0.62 $\mu V/\sqrt{Hz}$, matching the expected value of 0.608 $\mu V/\sqrt{Hz}$. To determine the noise factor F of the APD, the noise floor is measured at increasing optical powers at a bias of 50 V. These data are fit to Eq. 3.10 with a least squares optimization with F as a free parameter. This suggests that $F = 6.15$ with a 99.4 R^2 correlation coefficient. The data and the fit are seen in Fig. 3-16 a. The noise floor due to the dark current is also shown for comparison. Fig. 3-16 b shows the noise floor due to the dark current and the noise floor with 3n W of optical input. Even at this low optical input, the noise floor is 3x the dark current noise floor. Due to the large optical noise power inserted into the system, the optical power incident on the detector does not go below 3 nW. In fact, it will be well above 3 nW, up to 50 nW in high noise and high gain scenarios. Thus, the inherent noise in the direct detection system is low enough to ensure that the signal-to-noise ratio measurements are limited by the shot noise of the optical power created by the OPA.

3.8 Measurements

The quantum illumination setup built for this thesis is used to understand how an experimental implementation of QI compares to theory and to classical illumination. There are five free parameters in the system— the number of noise photons per mode (N_b), the number of signal entangled photons per mode (N_s), the amount of loss on the signal side (κ), the amount of loss on the idler side (μ), and the gain of the OPA (G). N_b is controlled through a fiber coupled attenuator. N_s is controlled by changing the pump power into the SPDC crystal. G is changed by placing a HWP before the OPA crystal which controls the amount of pump light polarized parallel to the crystal's z-axis. The amount of signal loss is controlled with a HWP and a PBS as discussed in Section 3.5.

3.9 Full Setup

Figure 3-17 shows the entire experimental setup including the lenses used for focusing into the SPDC crystal, reducing the beam waist into the phase modulator, and mode matching between the signal, pump, and idler beams at the OPA crystal.

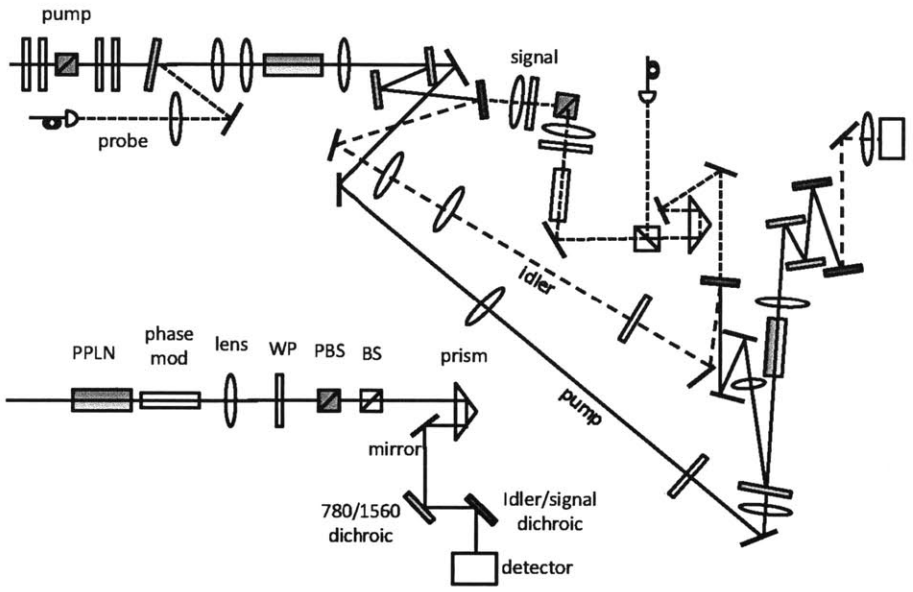

Figure 3-17: The full experimental setup.

3.10 Classical Illumination

Though not tested in this thesis, the balanced homodyne detection system for classical illumination can be implemented almost entirely in fiber for ease of alignment. A schematic is shown in Fig. 3-18. To create a classical illumination setup that is analogous to the QI case, the total power of the initial signal is matched and the power density of the noise is matched. A tunable Agilent laser is used at 1550 nm. This laser has an extremely narrow bandwidth of 0.16 pm (FWHM).

The LO is split from the signal with a 99:1 BS. The same phase modulator used in QI is used here (Section 3.2) because fiber coupled phase modulators are often extremely fast, and the modulation frequency must be well within the bandwidth of

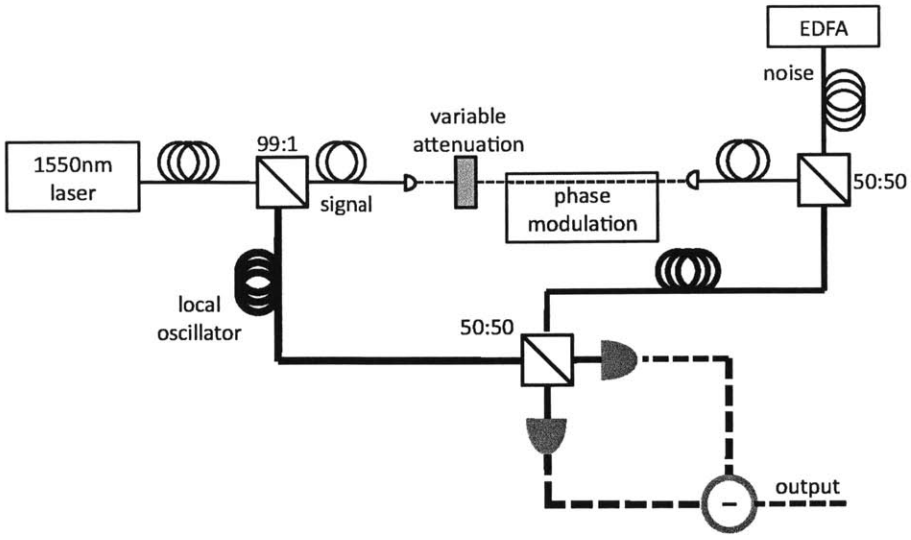

Figure 3-18: A schematic of the experimental setup of target detection with classical illumination and balanced homodyne detection.

the detector used. Loss is not an issue on the signal side, so coupling in and out of the single mode fiber is not a problem. The signal is further attenuated with a half wave plate and a polarized beam splitter in free space to achieve the desired level of signal at the receiver.

The noise is created by an un-seeded erbium doped fiber amplifier (EDFA). The broadband power spectrum created by an un-pumped EDFA is shown in Fig. 3-19. The amount of noise created by the EDFA is controlled by changing the current of the amplifier. This noise power is passed through a coarse wavelength division multiplexer (CWDM) filter centered at 1550 nm to reduce the overall power sent to the homodyne detection system. Noise power outside of the LO spectral bandwidth will not have an effect on the signal out of the homodyne detector, so strict filtering is not necessary. The power from the EDFA is randomly polarized. This is not an issue as it will not interact with the LO no matter what due to phase incoherence.

The noise from the EDFA is combined with the signal in a fiber coupled 50:50 BS. The LO is sent through a set of paddle polarizers to match the polarization of the signal for maximal interference. The return signal, consisting of a small phase modulated signal in a large bath of noise is combined with the polarization-matched

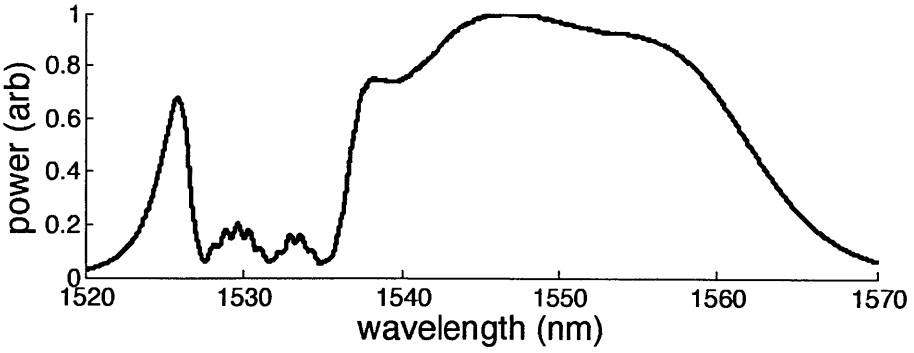

Figure 3-19: The scaled power spectrum of the un-pumped EDFA.

local oscillator in a final 50:50 BS. The two output ports of this 50:50 BS are measured by a pair of fiber coupled balanced photodetectors and the currents from these two detectors are subtracted to calculate the output of the homodyne receiver. The photodetection system used is an auto-balanced photoreceiver from NewFocus (Nirvana, Model 2017) with 50 dB common mode rejection, a gain of 1×10^6, and a responsivity of 1 A/W at 1550 nm.

Chapter 4

Experimental Results

The signal strength and noise level of the implementation of target detection based on quantum illumination discussed in Chap. 3 is measured under various conditions. The phase of the signal is modulated at 16 kHz and an audio Network Analyzer is used to examine the frequency spectrum of the signal created by the OPA. For all measurements, a 1.56 kHz window consisting of 400 frequency bins, each with a linewidth of 3.9 Hz. The spectrum is centered on 16 kHz. The Network Analyzer uses a Hanning window function. The power spectrum density of the signal is measured to account for the video bandwidth of the analyzer and the window function.

Fig. 4-1 shows sample frequency spectra of the OPA output when a target is present and absent, respectively. In the measurement shown here, $N_b = 50$, $N_s = 0.0025$, $\kappa = 0.05$, $\mu = 0.8$, $M = 1.45 \times 10^{12}$ and the OPA gain is 1.0031 (with a pump power of 300mW at the crystal). With these parameters, the DC level of the optical power at the detector is approximately 35 nW. These spectra are single-shot measurements, taken without averaging. When a target is present, a peak is seen at the modulation frequency of the phase due to the phase-sensitive interaction between the signal, idler, and pump beams at the OPA. When there is no target present, there is no peak created because the phase-modulated signal does not reach the detector. Only noise is present, dominated by the shot noise due to the power created at the idler wavelength due to the interaction between the pump and noise beams.

The phase of the signal and idler beams fluctuate due to air turbulence and thus

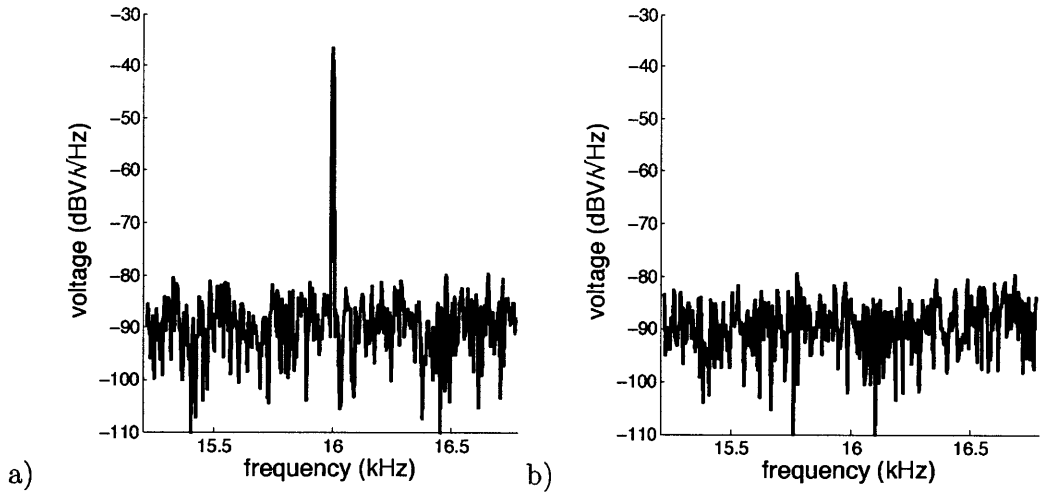

Figure 4-1: a) Measured spectrum with a target present, leading to a strong peak at the modulation frequency. b) Measured spectrum with no target present and thus no peak at the modulation frequncy, only shot noise. $N_b = 50$, $N_s = 0.0025$, $\kappa = 0.05$, $\mu = 0.8$, $M = 1.45 \times 10^{12}$, and $G = 1.0031$.

the amplitude modulation created by the phase-dependent interaction at the OPA also fluctuates (see Sec. 3.2). To ensure that the maximum modulation is captured for each setting of G and κ, the peak is monitored over 5000 measurements, corresponding to approximately one minute and the maximum peak value is recorded. To accurately measure the noise floor, 500 measurements are averaged to reduce the amplitude fluctuations.

4.1 Interacting Idler Power

If the SPDC emission were entirely collinear to the pump, it would be possible to perfectly match the signal, idler, and pump modes at the OPA through standard focusing methods. However, as calculated in Section 3.1.1 and shown experimentally in Section 3.1.4, a large amount of the entangled power created through SPDC is not collinear to the pump. It is expected that this non-collinear SPDC emission will not be amplified as strongly at the OPA as there is no pump power in these spatial modes. To verify this, the strength of the modulated signal created by the OPA is measured under various conditions and compared with the expected signal.

In Sec. 3.4 it is calculated that $M = 1.45 \times 10^{12}$ temporal modes per second have larger than 50% visibility at the OPA. To find N_s, the number of entangled photons interacting at the OPA within each of these modes, the strength of the signal is measured for increasing OPA gain for three different values of signal transmission κ. These data are matched to the expected dependence through a least squares optimization with N_s as the free parameter. The expected signal strength is given by

$$2V_{AC} = 4M\sqrt{G(G-1)\kappa\mu N_s(N_s+1)}\,\frac{hc}{\lambda_i}R_f M_{\text{apd}}. \tag{4.1}$$

The SPDC crystal is pumped with 400 mW of power, and 5 nW of the idler output power is measured at the OPA using the InGaAs detector. Signal measurements are taken for three known levels of signal transmission $\kappa = 0.25$, 0.05, and 0.005 as the pump power at the OPA is increased. The dependence of G, the OPA gain, on pump power P_p is given by $G = 1 + P_p\,0.0102$ as found through DFG in section 3.6.2.

Each of the three sets of data obtain from the measurements (data points shown in Fig. 4-2) is fit to Eq. 4.1 separately with a least squares optimization with $M = 1.45 \times 10^{12}$, $\mu = 0.8$, and the measured κ values (0.25, 0.05, 0.005). N_s is the free parameter used to fit the equation to each set of data separately. It is found that $N_s = 25 \pm 2 \times 10^{-4}$ from the N_s values from the three sets of data. Along with the measured data points, Figure 4-2 shows the expected dependence of the AC signal on pump power using $N_s = 25 \times 10^{-4}$, $M = 1.45 \times 10^{12}$, $\mu = 0.8$, and $G = 1 + P_p\,0.0102$ for $\kappa = 0.25$, 0.05, and 0.005.

The value of N_s suggests that only $P_{\text{eff}} = \frac{MN_s hc}{\lambda_i} = 0.48\,\text{nW}$ of the 5nW of idler power interacts at the OPA. This is only 9.6% of the total idler power. To verify that the discrepancy between the total idler power and the effective idler power P_{eff} is, in fact due to non-collinear emission, a pinhole is placed in the idler path in the hopes of clipping a portion of the non-collinear power while retaining all the collinear power. To eliminate the maximum amount of non-collinear power while avoiding clipping of the collinear power, a pinhole should be placed at a focus point along the idler path as determined by a probe beam. At this point, the power in the fundamental mode

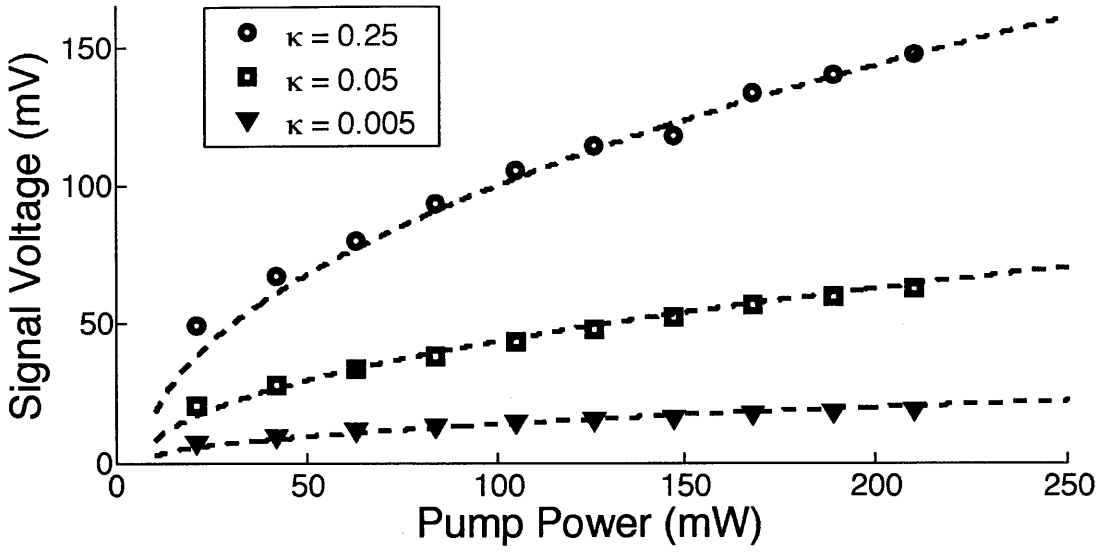

Figure 4-2: Measured signal strength for 400 mW of pump power at the SPDC crystal, $M = 1.45 \times 10^{12}$, $\mu = 0.8$, and $G = 1 + P_p\, 0.0102$ for $\kappa = 0.25$, 0.05, and 0.005. Expected V_{AC} with $N_s = 25 \times 10^{-4}$ as found though a least squares optimization of Eq. 4.1 to the measured data.

will be concentrated within the small beam waist whereas the other modes may not be focused. There is one focus point on the idler path outside of the crystals. At this point, the beam waist $w_0 = 80\,\mu$m.

The SPDC crystal is pumped with 450 mW of power and with no spatial filtering, 5.6 nW of idler power is obtained at the detector and a QI signal of 0.55 nW_{pp} is detected. A 200 μm pinhole placed at the 80 μm focus reduces the signal, due to clipping of the collinear power. The next larger pinhole available is 500 μm. This is, unfortunately, too large and clips neither the total idler power or the QI signal. This pinhole is translated along the beam path and the noise and signal powers are measured at each increment. The idler power begins to be clipped outside the Rayleigh range. The pinhole is translated until the signal power begins to drop. Immediately before this location, 2.46 nW of idler power is obtained at the detector and the QI signal is the same, 055nW_{pp}. These data show that at most 44% of the idler power interacts with the pump at the OPA. Interestingly, the aperture position at which the signal begins to drop is the point at which a probe beam begins to be

clipped. This supports the theory that single mode emission experiences the highest gain at the OPA. Of course, there is power in non-collinear modes that is within the spatial extent of the collinear emission so it is impossible to completely filter the non-interacting modes in this way.

Furthermore, as seen in Section 3.1.4, a 20 nm filter centered at the collinear wavelength lowers the power considerably at the detector, suggesting that only 20% of the overall emission is within that bandwidth. As found in Section 3.4, the spectral bandwidth of the interacting photons is $\Delta\lambda_s = 13\,\text{nm}$ and $\Delta\lambda_i = 10.86\,\text{nm}$. By comparing the spectral distribution of the interacting photons to the filter, it is calculated that 20% of the total idler power is within the interacting bandwidth. This calculation suggests that not more than 20% of the entangled power incident on the OPA can be amplified. Of course, not all the power within that bandwidth is collinear, so not all of it will be amplified at the OPA.

The multi-spatial mode composition of the SPDC emission accounts for the majority of the discrepancy between the detected idler power and P_{eff}, the amount of idler power which contributes to the signal. However, non-optimal alignment and mode matching of the fundamental mode containing the collinear emission also reduces the amount of signal created at the OPA. An initial alignment and mode matching is done with probe beams as discussed in chapter 3. Further alignment is done while monitoring the signal. However, this is a slow and imprecise process due to the fluctuations of the signal due to phase instability, and it is possible that the optimal alignment and mode matching has not been found.

4.2 Measured DC Level and Noise Floor

After gaining and understanding of how the signal created by the quantum illumination setup relates to the signal expected theoretically, it is important to relate the DC level and noise floor to the expected values. They are measured for various levels

of pump power and these measurements are compared with the expected DC level,

$$V_{DC} = M\left(G\mu Ns + (G-1)(\kappa N_s + N_b + 1)\right) R_f M_{\text{apd}} + P_{\text{ex}} R_f M_{\text{apd}} \tag{4.2}$$

and the noise due to this DC level,

$$\sigma_N = \sqrt{N_{\text{det}}^2 + N_{sh_{\text{dark}}}^2 + N_{sh_{\text{DC}}}^2} \tag{4.3}$$

or the square root of the sum of the squares of the detector noise, the shot noise due to the dark current, and the shot noise due to the expected DC level (V_{DC}). The last term in Eqn. 4.3 is due to the excess idler power which does not interact at the OPA but is still incident at the detector. It is determined by fitting the signal to the expected signal to find P_{eff} as described in Sec. 4.1. The excess idler power, $P_{\text{ex}} = P_i - P_{\text{eff}}$. The noise power P_n at the OPA is known, and the number of noise photons per temporal mode is found through $P_n = MN_b\frac{hc}{\lambda_s}$. The full noise characteristics of the direct detection system discussed in Sec. 3.7 are taken into account when calculating the expected noise floor.

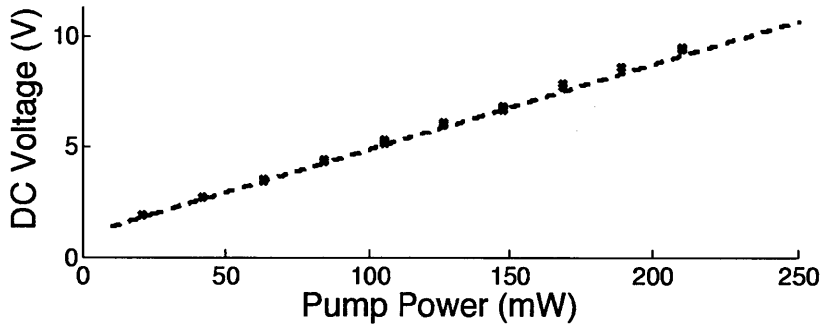

Figure 4-3: Measured and expected DC power with $N_b = 97.6$, $M = 1.45 \times 10^{12}$, $\kappa = 0.05$, $\mu = 0.8$, $N_s = 0.0025$ for increasing pump power.

Three rounds of measurements are taken with 17 μW of noise power entering the OPA to achieve approximately 100 photons per mode ($N_b = 97.6$). As seen in Fig. 4-3, the measured data fits extremely well the expected DC level calculated with $N_b = 97.6$, $M = 1.45 \times 10^{12}$, $\kappa = 0.05$, $\mu = 0.8$, $G = 1 + P_p\,0.0102$ and $N_s = 0.0025$

(as found in Section 4.1). All of the noise power must then interact with the pump at the OPA, suggesting that the alignment and mode matching of the noise beam and the pump beam is extremely good. This finding supports the theory that the small P_{eff} found in Sec. 4.1 is overwhelmingly due to a lack of OPA gain in the non-collinear modes and not to misalignment or faulty fundamental mode matching. Moreover, the noise floor matches the expected noise floor as seen in Fig. 4-4 confirming that there are no unexpected sources of noise. The variation in the measured data is due to fluctuations in the polarization of the diode laser used to inject noise into the system.

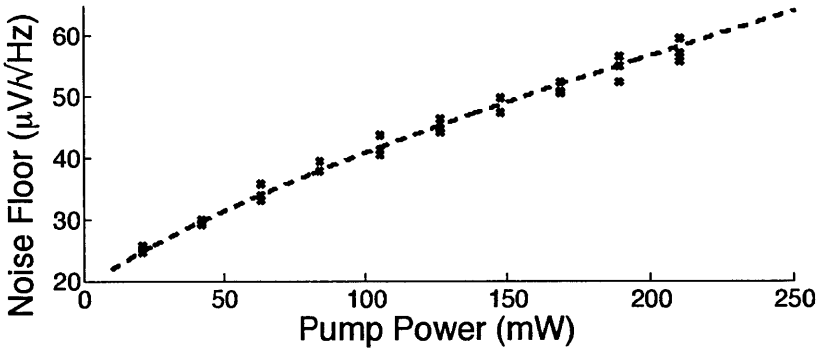

Figure 4-4: Measured and expected noise floor with $N_b = 97.6$, $M = 1.45 \times 10^{12}$, $\kappa = 0.05$, $\mu = 0.8$, $N_s = 0.0025$ for increasing pump power.

4.3 Measured Signal to Noise Ratio

Armed with an understanding of the signal and noise, the SNR of this initial quantum illumination experiment is tested. Figure 4-5 shows the data points of the measured SNR for $\kappa = 0.25$, 0.05, and 0.005 with $N_b = 97.6$ and $\mu = 0.8$. The dashed lines shows the calculated SNR,

$$\text{SNR} = 10\log_{10}\left(\frac{V_{AC}}{\sigma_N}\right)^2 \tag{4.4}$$

with $\kappa = 0.25$, 0.05, and 0.005. $N_b = 97.6$, $\mu = 0.8$, $G = 1 + P_p\, 0.0102$ and $N_s = 0.0025$ (as found in Section 4.1).The solid line in Fig. 4-5 shows the expected SNR if $P_{\text{ex}} = 0$,

or if all the excess idler power that does not interact at the OPA could be filtered, either spatially or spectrally. As seen, the expected SNR levels with and without excess idler power approach the same value for higher pump powers because the noise power due to the injected noise photons overwhelms P_{ex}.

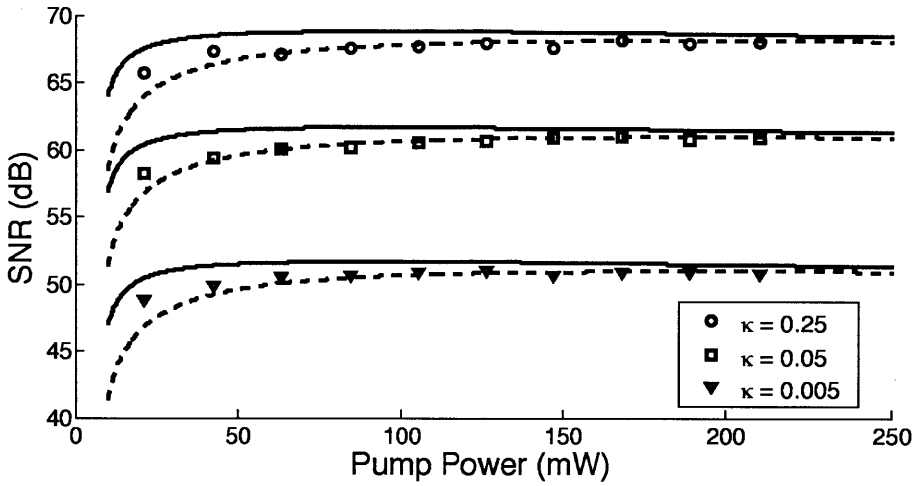

Figure 4-5: The measured and expected effect of κ on the SNR of target detection based on quantum illumination $N_b = 97.6$, $M = 1.45 \times 10^{12}$, $\mu = 0.8$, $N_s = 0.0025$. The solid lines are the expected SNR with the same parameters, but with $P_{ex} = 0$.

Figure 4-6 shows the measured SNR data points with $17\,\mu$W, $10\,\mu$W and $5\,\mu$W of noise power at the OPA to provide approximately 100, 55, and 40 noise photons per mode, respectively ($\kappa = 0.05$, and $\mu = 0.8$). The dashed lines show the SNR calculated through Eq. 4.4 with $\kappa = 0.05$, $M = 1.45 \times 10^{12}$, $\mu = 0.8$, $G = 1 + P_p\, 0.0102$, and $N_s = 0.0025$ (as found in Section 4.1). The measured data match quite well with the expected SNR when the excess idler power is taken into account.

4.4 Conclusion

The data presented in this thesis clearly shows that a strong correlation remains between the idler and the return signal with the presence of a target, even when noise photons overwhelm the small number of signal photons returning to the detector. This correlation exhibits the expected dependence on the amount of signal lost in

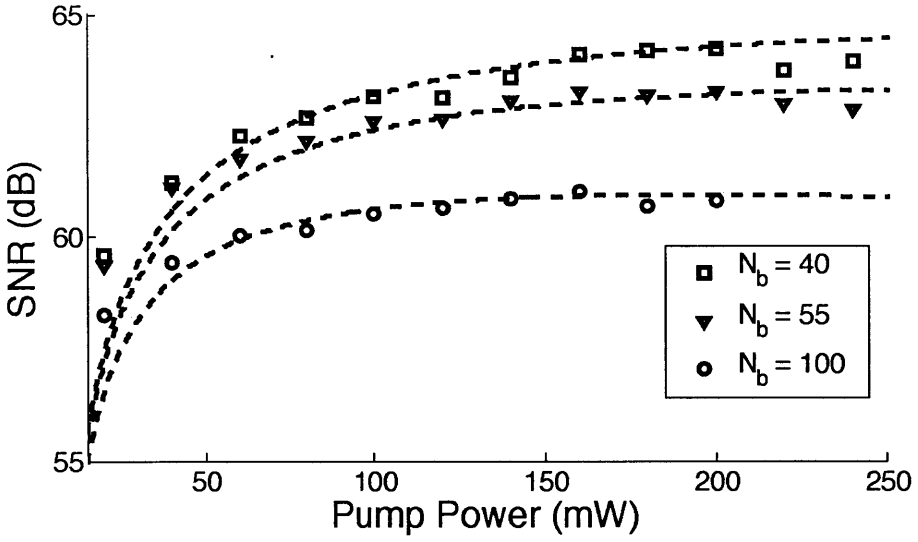

Figure 4-6: The measured and expected effect of N_b on the SNR of target detection based on quantum illumination $\kappa = 0.05$, $M = 1.45 \times 10^{12}$, $\mu = 0.8$, $N_s = 0.0025$.

transit. The noise in the system also scales as expected with the amount of gain at the OPA, and the number of noise photons per mode, confirming that there are no unexpected sources of noise in the system.

However, the SNR of target detection enhanced by quantum illumination is compromised by the highly multi-spatial mode content of the SPDC emission. This limits the SNR as the non-interacting idler raises the DC and noise floor levels while not contributing to the signal. There are two approaches to fixing this. The extraneous idler could be blocked either spectrally or spatially. This would limit the extra DC noise, improving the SNR considerably - especially at low noise powers. With initial spatial filtering, it has been shown that the total idler power incident on the OPA can be halved while retaining the same SNR of the O PA output. Ideally, the emission of the SPDC would be improved such that a larger percentage of the power created through SPDC is collinear to the pump and thus able to experience the optimal gain at the OPA.

To ensure a fair comparison between the quantum and classical illumination cases, the amount of signal and idler power interacting at the OPA must be known precisely. In the experimental setup presented in this thesis, this unfortunately cannot be deter-

mined exactly. In the future extension of this work, the signal power will be coupled to a single mode fiber. This will ensure that all of the signal power will interact at the OPA. Then only the return signal powers for the QI and classical illumination setups must be matched.

With further filtering, or improvement of the single mode content of the SPDC, a fair comparison between the two setups can be made. The preliminary data presented in this thesis strongly suggests that this comparison would reveal the SNR enhancement through quantum illumination expected by theory.

Bibliography

[1] Ryan S Bennink. Optimal collinear gaussian beams for spontaneous parametric down-conversion. *Phys. Rev. A*, 81:053805, May 2010.

[2] G.D. Boyd and D. A. Kleinman. Parametric interaction of focused gaussian light beams. *Journal of Applied Physics*, 39(8):3597–3639, 1968.

[3] R. L. Byer and S. E. Harris. Power and bandwidth of spontaneous parametric emission. *Phys. Rev.*, 168:1064–1068, Apr 1968.

[4] P.A. Franken, A.E. Hill, C.W.Peters, and G. Weinreich. Generation of optical harmonics. *Phys. Rev. Lett.*, 7:118–119, Aug 1961.

[5] Vittorio Giovannetti, Seth Lloyd, and Lorenzo Maccone. Quantum-enhanced measurements: Beating the standard quantum limit. *Science*, 306(5700):1330–1336, 2004.

[6] Saikat Guha. Receiver design to harness quantum illumination advantage. *ISIT*, pages 963–967, 2009.

[7] Saikat Guha and Baris I. Erkmen. Gaussian-state quantum-illumination receivers for target detection. *Phys. Rev. A*, 80:052310, Nov 2009.

[8] Thomas Jennewein, Christoph Simon, Gregor Weihs, Harald Weinfurter, and Anton Zeilinger. Quantum cryptography with entangled photons. *Phys. Rev. Lett.*, 84:4729–4732, May 2000.

[9] D. H. Jundt. Temperature-dependent sellmeier equation for the index of refraction, n_e, in congruent lithium niobate. *Optics Letters*, 22:1553–1555, 1997.

[10] B. Lai. A tunable light source at $1.6\,\mu$ by difference-frequency mixing in cesium titanyl arsenate. *M.S. thesis M.I.T. E.E.C.S.*, 1995.

[11] B. Lai, N.C. Wong, and L.K. Cheng. Continuous-wave tunable light source at $1.6\,\mu$m by difference-frequency mixing in cstioaso$_4$. *Optics Letters*, 20:1779–1781, September 1995.

[12] Daniel Ljunggren and Maria Tengner. Optimal focusing for maximal collection of entangled narrow-band photon pairs into single-mode fibers. *Phys. Rev. A*, 72:062301, Dec 2005.

[13] Seth Lloyd. Enhanced sensitivity of photodetection via quantum illumination. *Science*, 321:1463–1465, 2008.

[14] R.J. McIntyre. Multiplication noise in uniform avalanche diodes. *IEEE Trans. Electron Devices.*, ED-13:164–168, 1996.

[15] Jeffrey H. Shapiro and Seth Lloyd. Quantum illumination versus coherent-state target detection. *New Journal of Physics*, 11(6):063045–060349, 2009.

[16] Peter W. Shor. Polynomial-time algorithms for prime factorization and discrete logarithms on a quantum computer. *SIAM J. Comput.*, 26(5):1484–1509, 1997.

[17] Si-Hui Tan, Baris I. Erkmen, Vittorio Giovannetti, Saikat Guha, Seth Lloyd, Lorenzo Maccone, Stefano Pirandola, and Jeffrey H. Shapiro. Quantum illumination with gaussian states. *Phys. Review Letters*, 101:253601, 2008.

[18] H. P. Yuen and V. W. S. Chan. Noise in homodyne and heterodyne detection. *Opt. Lett.*, 8(3):177–179, Mar 1983.